*J. Fluid Mech.* (2024), *vol*. 996, A5, doi:10.1017/jfm.2024.694

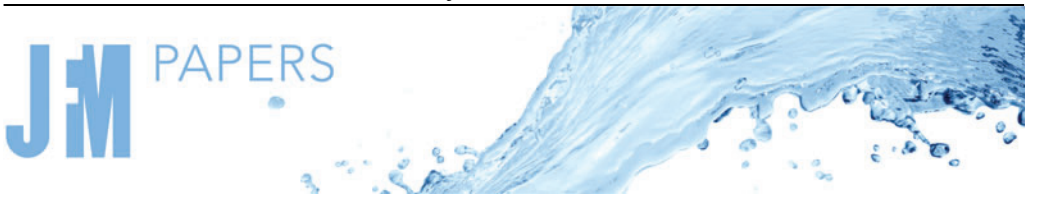


# The use of patterned heating in controlling pressure losses within sloping channels

**J.M. Floryan**[1],†, **W. Wang**[1] **and Andrew P. Bassom**[2]

[1]Department of Mechanical and Materials Engineering, The University of Western Ontario, London, Ontario N6A 5B9, Canada

[2]School of Natural Sciences, University of Tasmania, Private Bag 37, Hobart, TAS 7001, Australia

(Received 28 November 2023; revised 26 June 2024; accepted 26 June 2024)

The effectiveness of utilizing heating patterns as a drag-reduction tool in sloping channels is analysed. The usefulness of heating is judged by determining the pressure gradient required to maintain the same flow rate as in the isothermal case. The key to reducing pressure loss is the formation of separation bubbles, although these bubbles are washed away at relatively large Reynolds numbers. The bubbles reduce the direct contact between the stream and the side walls, thereby reducing the friction experienced by the flow. Moreover, the fluid inside the bubbles tends to rotate, a motion provoked by longitudinal temperature gradients. This rotation also seems to reduce the resistance. On the other hand, the existence of the bubbles tends to obstruct the stream, increasing the flow resistance. In general, channels oriented close to horizontal experience a relatively small pressure loss, but this loss grows markedly as the channel inclines towards the vertical. When modest heating is applied, the pressure loss is approximately proportional to the square of the associated Rayleigh number. It is also shown that if the heating wavelength is too short or too long, the heating loses its effectiveness. In certain circumstances, it turns out that the theoretical pressure-gradient reduction achieved by judicious heating is so large that it exceeds the pressure gradient required to drive the flow in the isothermal problem. The conclusion is that in these instances, a pressure gradient of the opposite sign must be applied to prevent flow acceleration.

**Key words:** drag reduction

† Email address for correspondence: floryan@uwo.ca

## 1. Introduction

Ever-increasing energy costs are a primary motivation for the continuing interest in developing techniques that reduce pressure losses in conduits. Two principal sources of loss can arise from pressure interaction with any wall topography and the friction between the fluid and the bounding wall. Mohammadi & Floryan (2012) summarize the pressure-loss mechanisms, and some techniques for its reduction are known. While the mechanisms underpinning friction are now well understood, knowledge of effective methods for its reduction is less well developed. Here, we examine the role that spatially distributed heating could play in limiting pressure losses.

The friction generated at the wall of a channel by a fluid flowing through it is a joint function of the fluid viscosity and the wall-normal velocity gradient. Assuming that the working fluid cannot be changed, the friction can be reduced only by modifying the near-wall velocity field, and how this might be done depends on whether the flow is laminar or turbulent. If the flow is turbulent or in danger of becoming turbulent, one might appeal to a suitable control strategy designed either to relaminarize an already turbulent flow or to delay the transition. We shall not pursue these ideas but instead focus on problems in which the flow is laminar. Given this, we further remark that flow modifications that might reduce friction can be created using either passive or active processes. There has been considerable research into active systems that rely on various actuators. Examples of studies include investigations using plasma (Inasawa, Ninomiya & Asai 2013), sound (Kato, Fukunishi & Kobayashi 1997), piezo elements (Fukunishi & Ebina 2001) or transpiration (Min *et al.* 2006; Bewley 2009; Fukagata, Sugiyama & Kasagi 2009; Hoepffner & Fukagata 2009; Mamori, Iwamoto & Murata 2014; Jiao & Floryan 2021*a*,*b*). Unfortunately, none of these seem able to achieve net energy savings. More positively, though, it has been shown recently that a combination of transpiration and an in-plane wall motion (Floryan 2023) may give a better outcome.

One can view these active modulations as propulsion-assisting methods in which energy is expended on the actuation rather than increasing a classical propulsive force. Further work on force reduction arises in the emerging field of vibration-based resistance limitation and/or distributed propulsion, especially the use of small-amplitude fast waves which rely on the peristaltic effect (Floryan & Zandi 2019; Floryan & Haq 2022; Haq & Floryan 2022, 2023; Floryan, Haq & Bassom 2023*a*,*b*).

In many ways, passive processes might be preferable to active ones as they do not require any energy input. An obvious way to reduce the friction would be to modify appropriately the surface topography of the wall. A smooth surface is often thought to provide the lowest possible friction, as any modifications in surface topography would increase the wetted area. If the surface were perturbed away from being flat, an overall lessening of friction could only be achieved if the increase in the friction area was compensated for by a sufficiently large reduction in the shear. Longitudinal grooves are known to reduce drag through changes in the distribution of the bulk flow (Mohammadi & Floryan 2013*a*, 2014, 2015; Moradi & Floryan 2013). The topography of the grooves can be optimized (Mohammadi & Floryan 2013*b*; Moradi & Floryan 2013) with the ideal shape determined by the constraints imposed. The stability limits of such flows have been well documented (Moradi & Floryan 2013, 2014; Mohammadi, Moradi & Floryan 2015). Another class of grooves, known as riblets (Walsh 1983), is characterized by being of very short wavelength, but these are prone to contamination. This contamination can result in clogging and destruction if exposed to shear for extended periods. Riblets are often used in turbulent flows but are rarely chosen in laminar circumstances (Mohammadi & Floryan 2013*a*).

Superhydrophobic effects (Rothstein 2010) offer an alternative route for passive drag reduction. These surfaces trap gas bubbles in micropores, thereby replacing direct liquid–solid contact with gas–liquid contact, which in turn reduces the friction experienced by the liquid. This method is intrinsically limited to two-phase flows, and its effectiveness is limited by the pressure drag associated with surface irregularities (Ou, Perot & Rothstein 2004; Joseph *et al.* 2006; Truesdell *et al.* 2006; Aljallis *et al.* 2013; Park, Park & Kim 2013; Srinivasan *et al.* 2013; Park, Sun & Kim 2014). Its potency can be increased in several ways: there is an advantage to be gained by suitably shaping the surface pores, enhancing the hydrophobicity through surface chemistry, increasing the surface tension, fixing the position of contact points through geometric means or controlling the contact angles (Quéré 2008; Reyssat, Yeomans & Quéré 2008; Samaha, Tafreshi & Gad-el-Hak 2011, 2012). Caution needs to be exercised as there is the potential for shear-driven or interfacial instabilities to occur, and excess hydrostatic pressure can lead to a collapse of the gas bubbles. In this case, the liquid is directly exposed to the rough surface (Poetes *et al.* 2010; Bocquet & Lauga 2011; Zhou *et al.* 2011; Aljallis *et al.* 2013). The micropores need to be extremely small to provide stable interfaces, which, as noted earlier in the context of riblets, makes them prone to damage through clogging. If the gas is replaced with some other immiscible liquid, this prevents bubble collapse and gives rise to liquid-infused surfaces (Wong *et al.* 2011). An overall drag reduction is still possible despite the infusing liquid having a much higher viscosity than the gas it replaces (Solomon, Khalil & Varanasi 2014, 2016; Rosenberg *et al.* 2016). This technique suffers from the drawback that the pressure variations along the surface are liable to wash away the infusing liquid (Van Buren & Smits 2017).

Our primary interest in this work is in using spatial heating patterns to influence the friction on the wall through the generation of convection rolls. Three effects come into play. First, the rolls reduce the direct contact between the stream and the bounding walls, reducing resistance. Moreover, density gradients drive the fluid rotation inside the rolls and provide a propulsive force that promotes fluid movement. Unfortunately, the rolls also reduce the cross-sectional area of the flow, so it is difficult to predict the net result *a priori*. Several studies in horizontal channels found reduced pressure losses (Hossain, Floryan & Floryan 2012; Hossain & Floryan 2014, 2016; Floryan & Floryan 2015; Inasawa, Taneda & Floryan 2019). When used in vertical channels, the reductions strongly depend on the Prandtl number as the flow-induced break of thermal symmetries generates a buoyancy force acting along the flow (Floryan, Wang & Bassom 2023*d*). It is not known how flows in inclined channels may react to the patterned heating as the magnitude of the axial component of the buoyancy force changes markedly with the channel inclination angle. The addition of a groove pattern amplifies this effect if the location of the grooves is carefully chosen relative to the positions of the rolls (Abtahi & Floryan 2017*a*,*b*, 2018; Floryan & Inasawa 2021; Inasawa, Hara & Floryan 2021). This enhancement is a demonstration of the so-called pattern interaction effect (Abtahi & Floryan 2017*a*,*b*, 2018; Floryan & Inasawa 2021; Inasawa *et al.* 2021), whose magnitude has been detailed by Hossain & Floryan (2020). Spatial heating patterning has been shown to reduce the forces between plates in relative motion (Floryan, Shadman & Hossain 2018), creating propulsion (Floryan, Panday & Aman 2023*c*; Floryan *et al.* 2023*d*; Floryan, Aman, & Panday 2024) and the ability for fluid pumping (Hossain & Floryan 2023). Information about the stability limits of such flows is sparse (Hossain & Floryan 2013*b*, 2015*b*, 2022).

Spatial heating patterning can be used to create the so-called chimney effect in non-vertical openings. This effect involves using natural convection in vertical channels to evacuate combustion gases from fireplaces (Putnam 1882). It is of significant interest

in architectural design as it provides passive ventilation, whereby heated air flows upward and draws in cool air at the base of a structure (Linden 1999; Wong & Heryanto 2004; Mortensen *et al.* 2011; Nagler 2021). A reverse effect can also occur when relatively hot air is brought down from above into a cooler environment. Vertical openings are important in designing various fire prevention measures owing to the possibility of controlling the intensification of combustion and the spreading of fires (Song *et al.* 2020). Upright fault lines are known to be significant in the context of thermal recovery processes (Tournier, Gethon & Rabinowicz 2000). More contemporary uses of the chimney effect include the passive cooling of electronic components (Naylor, Floryan & Tarasuk 1991; Straatman, Tarasuk & Floryan 1993; Straatman *et al.* 1994; Novak & Floryan 1995; Shahin & Floryan 1999; Andreozzi, Buonomo & Manca 2005) as well as in the design of passively cooled nuclear reactors (Weil 2012). There is an obvious interest in assessing the effectiveness of the chimney effect in oblique openings.

Fundamental studies of vertical natural convection can be traced back to Zeldovich's (1937) and Batchelor's (1954) work, involving bounding surfaces kept at a constant temperature. They were followed by an analysis of the possible transition to secondary states (Vest & Arpaci 1969; Lee & Korpela 1983; Hall 2012), turbulent convection (Ng *et al.* 2015) and the effect of wall roughness (Shishkina & Wagner 2011; Toppaladoddi, Succi & Wettlaufer 2017). Further work has examined the modifications created by ratchet surfaces (Jiang *et al.* 2019). Using heating patterns to promote the chimney effect has attracted recent interest (Floryan *et al.* 2022*a*,*c*, 2023*c*,*d*; Floryan, Haq & Panday 2022*b*).

Given that these previous studies have demonstrated that reduced losses can be achieved using the chimney effect, we intend to characterize the flow response in a channel inclined to gravity and subjected to patterned heating. Such heating does not alter the mean temperature of channel walls but produces spatial modulations that may lead to the lowering of friction experienced by the fluid stream. Patterned heating is of interest as only relatively small heating levels can be sufficient to reduce significantly the pressure gradient required to maintain the desired flow rate.

The remainder of this paper is organized as follows. In § 2, we formulate the model problem that quantifies the flow response and discuss the numerical methods used later in the work. Section 3 describes the flow responses of the configuration when the applied heating is of a wavelength comparable to the width of the channel. The calculations here are restricted to when one of the walls is heated, but this is extended to account for both walls being heated; this is done in § 4. It is also noted that our problem can be analysed analytically when the applied heating is either of a long wavelength or of a short wavelength. These two limits are considered in §§ 5 and 6, respectively. We show excellent agreement between the theory and the computations in the appropriate limits, reinforcing confidence in both. The paper closes in § 7 with a summary of the main conclusions and some further remarks.

Lastly, we mention that it is well known that the quantitative details of convection are affected by the choice of the Prandtl number $Pr$ (Hossain & Floryan 2022; Floryan *et al.* 2023*d*). All our calculations are conducted with $Pr = 0.71$, which is the value appropriate to air; consequently, should the value of $Pr$ be altered, the finer details of the results are likely to change, but the global features are unlikely to be altered.

## 2. Formulation

Consider the steady, two-dimensional pressure-gradient-driven flow of a Boussinesq fluid in an isothermal channel of width $2h$ inclined at an angle $\beta$ to the horizontal, as shown in figure 1. We align the $x$ and $y$ coordinate axes parallel and perpendicular to the slot

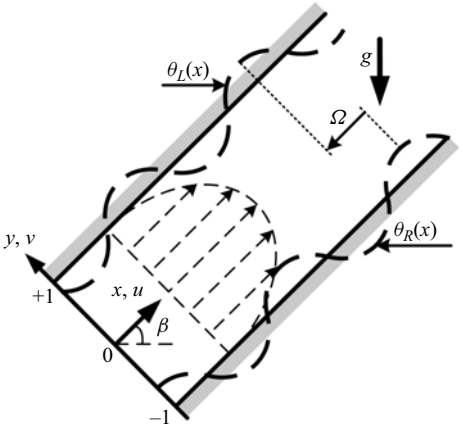


Figure 1. A schematic of the flow configuration in the slot defined by $|y| \leq 1$. The channel is inclined to the horizontal at an angle $\beta$ while the two walls are heated by sinusoidal thermal profiles defined by (2.4). These two profiles are offset by a phase $\Omega$.

and non-dimensionalize all lengths on the half-width $h$ so that the sides of the channel are given by $y = \pm 1$. In the absence of any fluid motion, there is a hydrostatic pressure $p_h(x, y)$ given by the solution of

$$\frac{\partial p_h}{\partial x} = -\rho g \sin\beta, \quad \frac{\partial p_h}{\partial y} = -\rho g \cos\ \beta, \tag{2.1a,b}$$

where $g$ is the gravitational acceleration and $\rho$ is the density of the fluid. When the fluid moves, the basic motion is given by velocity $\boldsymbol{v}_0(x, y)$ and pressure $p_0(x, y)$ fields, which are

$$\boldsymbol{v}_0(x, y) = (1 - y^2, 0), \quad p_0(x, y) = -2x/Re, \tag{2.2a,b}$$

where the velocity vector $\boldsymbol{v}_0 = (u_0, v_0)$ is scaled on the maximum of the $x$-velocity $u_{max}$ and $p_0$ is the pressure in excess of $p_h$ based on $\rho u_{max}^2$. The form of $p_0$ depends on the Reynolds number $Re \equiv u_{max}h/\nu$ with $\nu$ the kinematic viscosity. Given this basic flow, it is straightforward to find the associated stream function $\Psi_0$, the flow rate $Q_0$ through the slot and the shear force (per unit length and width) $F_{R0}$ ($F_{L0}$) acting on the fluid at the right (left) wall. These quantities are given by

$$\Psi_0 = y - \frac{y^3}{3} + \frac{2}{3}, \quad Q_0 = \frac{4}{3} \quad \text{and} \quad F_{R0} = F_{L0} = -2/Re. \tag{2.3a–c}$$

We next supply sinusoidal heating to both walls so that their scaled temperatures are given by

$$y = -1: \quad \theta_R(x) = \tfrac{1}{2} Ra_{p,R} \cos\alpha x, \tag{2.4a}$$

$$y = 1: \quad \theta_L(x) = \tfrac{1}{2}\ Ra_{p,L}\ \cos(\alpha x + \Omega), \tag{2.4b}$$

where the subscripts $R$ and $L$ denote the right and left walls, respectively. We remark that this periodic heating is applied to the surfaces throughout the domain; moreover, this profile is of wavenumber $\alpha$ (or wavelength $\lambda = 2\pi/\alpha$). We also remark that the two heating patterns at the two walls are offset by a phase angle $\Omega$. Here $\theta$ denotes the relative temperature defined by $T - T_R = \kappa\nu\theta/(g\Gamma h^3)$, where $T$ and $T_R$ denote the absolute and reference base temperature, respectively. Furthermore, $\kappa$ is the thermal diffusivity and $\Gamma$

is the thermal expansion coefficient, and we assume that fluid density variations follow the Boussinesq approximation. The appropriate Rayleigh numbers measure the intensity of the heating at the walls; on the right-hand side, we define $Ra_{p,R} = g\Gamma h^3\theta_{p,R}/(\kappa\nu)$, where $\theta_{p,R}$ is the magnitude of the applied heating with an analogous definition for $Ra_{p,L}$ relating to the left-hand edge of the slot. We mention in passing that it is well accepted that modelling buoyancy using the Boussinesq approach serves as an excellent paradigm for the underlying physics, especially when the temperature differences involved in the problem are relatively modest. For a discussion of the validity of this type of modelling, the interested reader is directed to the recent review by Mayeli & Sheard (2021).

The continuity, Navier–Stokes and energy equations govern the system. Written in terms of the dimensionless variables, we have

$$u\frac{\partial u}{\partial x} + v\frac{\partial u}{\partial y} = -\frac{\partial p}{\partial x} + \nabla^2 u + Pr^{-1}\theta\sin\beta, \quad \frac{\partial u}{\partial x} + \frac{\partial v}{\partial y} = 0, \tag{2.5a,b}$$

$$u\frac{\partial v}{\partial x} + v\frac{\partial v}{\partial y} = -\frac{\partial p}{\partial y} + \nabla^2 v + Pr^{-1}\theta\cos\beta, \quad u\frac{\partial \theta}{\partial x} + v\frac{\partial \theta}{\partial y} = Pr^{-1}\nabla^2\theta, \tag{2.5c,d}$$

where $(u, v)$ are the velocity components in the $(x, y)$ directions, respectively, scaled on $U_v = \nu/h$, $p$ is the pressure associated with fluid movement scaled with $\rho U_v^2$ and $\theta$ is the temperature; finally, $Pr = \nu/\kappa$ is the Prandtl number. (The generalization of the field equations to non-Boussinesq fluids may be found in the text by Tritton (1977).) The range of heating parameters used in the analysis is similar to that used in experiments reported by Inasawa *et al.* (2019, 2021) and Floryan & Inasawa (2021). A very good agreement between experimental data and theory was reported, demonstrating that the Boussinesq approximation captures a fluid response well. The required boundary conditions are

$$u(-1) = u(+1) = 0, \quad v(-1) = v(+1) = 0, \quad \theta(-1) = \theta_R(x) \quad \text{and} \quad \theta(+1) = \theta_L(x). \tag{2.6a–d}$$

We decompose the flow fields according to

$$u(x, y) = Re\, u_0(y) + u_1(x, y), \quad v(x, y) = v_1(x, y), \quad \theta(x, y) = \theta_1(x, y), \tag{2.7a–c}$$

$$p(x, y) = Re^2 p_0(x) + Bx + p_1(x, y), \quad \psi(x, y) = Re\ \psi_0(y) + \psi_1(x, y), \tag{2.7d,e}$$

so that if no heating were applied to the walls, we would have all quantities with subscript 1 identically zero. Our concern lies in determining whether applied heating can reduce the pressure gradient required to maintain a specified flow rate. Accordingly, we impose the mass flow rate constraint of the form

$$Q(x)|_{mean} = \left(\int_{-1}^{1} u(x, y)\,\mathrm{d}y\right)\bigg|_{mean} = \frac{4}{3}Re, \tag{2.8}$$

and seek information as to the size of the mean pressure gradient

$$\left.\frac{\partial p}{\partial x}\right|_{mean} = -2Re + B, \tag{2.9}$$

where positive values of $B$ signify a reduction of pressure losses.

The system (2.3)–(2.7) was solved by expressing the velocity components using a stream function $\psi$ defined in the usual manner, i.e. $u = \partial\psi/\partial y$, $v = -\partial\psi/\partial x$, then eliminating pressure and using Fourier expansions in the $x$ direction and Chebyshev expansions in

the $y$ direction. A description of the algorithm and the benchmarking of its accuracy are described by Hossain *et al.* (2012); the reader is referred to that paper for extended details. The pressure field was normalized by bringing the mean value of its periodic component to zero while the mean Nusselt number $Nu_{av}$ was evaluated using

$$Nu_{av} = -\lambda^{-1} \int_{x_0}^{x_0+\lambda} \left. \frac{\partial \theta}{\partial y} \right|_{y=-1} \mathrm{d}x. \tag{2.10a}$$

With this definition, a positive value of $Nu_{av}$ means that the right wall is losing energy. The cost of moving energy within a wall to create the local cold and hot spots is difficult to assess, but it contributes to the overall energy costs. The quantity of energy that has to be moved along the wall can be determined by evaluating the horizontal heat fluxes between the hot and cold wall segments. These fluxes can be quantified in terms of heat leaving each wall per half-heating wavelength and expressed by the horizontal Nusselt number defined as

$$Nu_{h,R} = -2\lambda^{-1} \int_{-\lambda/4}^{\lambda/4} \left. \frac{\partial \theta}{\partial y} \right|_{y=-1} \mathrm{d}x - Nu_{av}. \tag{2.10b}$$

This is not the only possible way to estimate the energy cost. Various alternatives have been suggested in the literature; the interested reader is directed to the papers by Maxworthy (1997), Siggers, Kerswell & Balmforth (2004), Hughes & Griffiths (2008) and Winters & Young (2009).

We remark that the shear forces acting on the fluid at the right and left walls are given by

$$F_R = -\lambda^{-1} \int_0^{\lambda} \left. \frac{\partial u}{\partial y} \right|_{y=-1} \mathrm{d}x, \quad F_L = \lambda^{-1} \int_0^{\lambda} \left. \frac{\partial u}{\partial y} \right|_{y=+1} \mathrm{d}x, \tag{2.11a,b}$$

and heating-induced changes of these forces are given as

$$\Delta F_R = F_R - Re^2 F_{R0}, \quad \Delta F_L = F_L - Re^2\, F_{L0}, \tag{2.12a,b}$$

with negative $\Delta F_R$ and $\Delta F_L$ corresponding to a reduction of these forces. The total (buoyancy) body force per unit length is given by

$$F_b = \lambda^{-1} Pr^{-1} \int_{-1}^{1} \int_0^{\lambda} \theta \, \mathrm{d}x \, \mathrm{d}y, \tag{2.13}$$

with its $x$ and $y$ components given by $F_{bx} = F_b \sin\beta$ and $F_{by} = F_b \cos\beta$, respectively.

It is noted that the above formulation is restricted to two-dimensional steady flows. There is always the possibility that the underlying structure may become time-dependent or that a secondary flow is set up. Some previous computations have addressed the question of the possibility of secondary structures in flows within horizontal channels (Hossain & Floryan 2013*b*, 2015*b*). Those findings suggest that no secondary flow appears unless $Ra_{p,R}$ is at least 2500. The results reported below are restricted to smaller Rayleigh numbers, so the complications that secondary structures would introduce ought not to arise.

## 3. Flow properties when one wall is heated

To begin our account of the effect of patterning on the pressure losses experienced along the channel, we consider the situation in which only one of the walls is heated. Within our problem, several parameters could be varied, but it is helpful to note that several

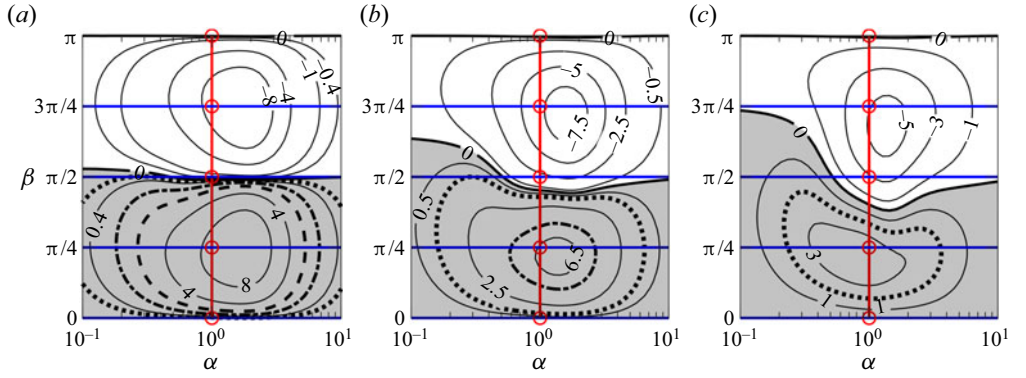


Figure 2. The variation of the pressure-gradient correction $B$ as a function of heating wavenumber $\alpha$ and slot inclination $\beta$ when only the right wall is heated with $Ra_{p,R} = 500$. In the three cases, the Reynolds number $Re =$ (*a*) 1, (*b*) 5 and (*c*) 10. The grey shading denotes parameter combinations corresponding to a reduction in pressure losses ($B > 0$). The thick dotted, dashed-dotted and dashed lines identify those conditions for which there are 10 %, 50 % and 100 % reductions of pressure losses, respectively. The circles mark the parameter choices used in figure 3, while the vertical red lines indicate the values adopted in figure 4. Finally, the horizontal blue lines identify the flow conditions used in figure 7.

inherent symmetries can be exploited to reduce the task. First, we need not be concerned about whether the flow is net upwards or downwards. If we transform $\beta \to \beta + \pi$ then the problem specification is unchanged if we switch the sign of $\theta$ and translate the coordinate $x \to x + (\pi/\alpha)$. We conclude that we can restrict the inclination of the channel $\beta \in [0, \pi]$. Furthermore, if one applies the transformations $(x, y, u, v, p, \theta, \beta) \mapsto (x, -y, u, -v, p, \theta, \pi - \beta)$ the governing equations are invariant while the boundary conditions swap over. This means that when it comes to considering the problem when only one wall is heated, we can examine the case when the patterning is applied to the right-hand wall so $Ra_{p,R} \neq 0$ and $Ra_{p,L} = 0$. We note in passing that these various symmetry properties have been confirmed by extensive numerical testing when the slot is horizontal (Hossain & Floryan 2014, 2015*a*).

The forms of the pressure losses as functions of the inclination angle $\beta$ and pattern wavenumber $\alpha$ are illustrated in figure 2 for three values of the Reynolds number $Re = 1$, 5 and 10; the interest in these particular values will become apparent as we proceed. It is noted that a reduction in the pressure losses can be achieved when $0 \leq \beta \leq \pi/2$; further, the critical inclination at which the reduction ceases to be possible is only weakly dependent on $\alpha$ when the Reynolds number is small (see figure 2*a*). As $Re$ is increased so the size of the parameter domain corresponding to a pressure reduction expands and does so especially at relatively long heating wavelengths; this is evident in figure 2(*b*,*c*). The heating leads to self-pumping at small $Re$ when an opposite pressure gradient must be applied to slow the fluid if the flow rate is to be maintained.

The forms of the flow and temperature fields as functions of the channel orientation $\beta$ and at Reynolds number up to 50 are shown in figure 3. (We point out that the flow conditions assumed for the three middle rows of this figure are marked with circles in figure 2.) The flow topology arises from a competition between the uniform isothermal Poiseuille flow in the positive $x$ direction and the natural convection driven by the applied periodic heating. Natural convection alone generates counter-rotating rolls, as illustrated in the first row of figure 3. The structure of these rolls does not change significantly as the orientation of the conduit is varied; it is seen that the fluid flows downward from cold spots and upward toward hot spots. The superposition of a small component of Poiseuille

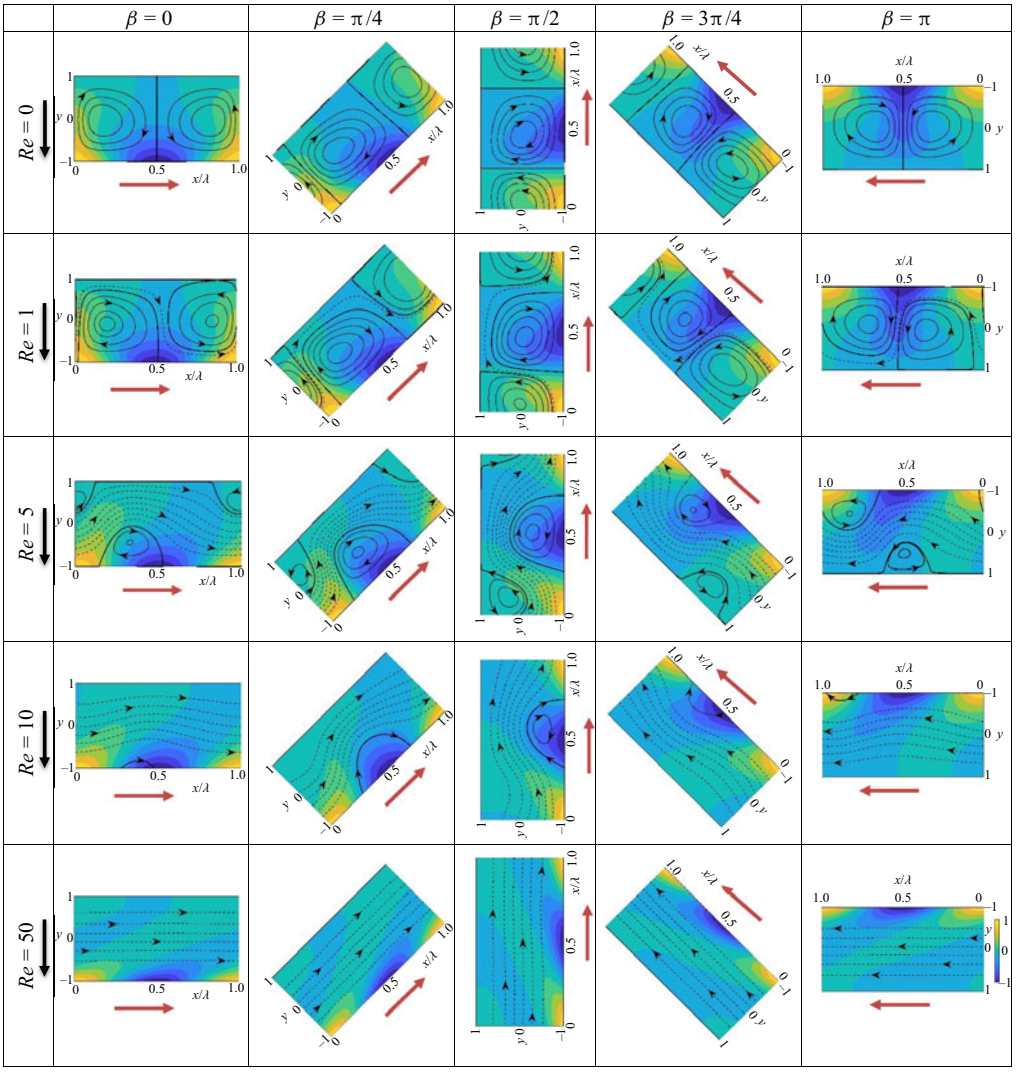


Figure 3. The flow and temperature fields for one-wall heating with $Ra_{p,R} = 500$ and a wavenumber $\alpha = 1$. The five rows of results correspond to $Re = 0$, 1, 5, 10 and 50, respectively. The downward black arrows show the direction of gravity force, while the red arrows indicate the direction of pressure-gradient force. The background colour illustrates the thermal field. The parameter choices used when $Re = 1$, 5 and 10 are marked in figure 2 by red circles, in figure 5 by green circles and in figure 7 by blue circles. In all the plots, the temperature has been normalized with its maximum $\theta_{max}$.

flow generates a thin stream tube that gently meanders between the rolls. As *Re* grows, we see an enlargement of the stream tube together with a slight reduction in the intensity of the rolls adjacent to the unheated wall. Further increase in *Re* leads to an ongoing thickening of the stream tube and the complete elimination of the upper rolls. At the point when these upper rolls completely disappear, those next to the lower (heated) wall have only undergone a relatively mild weakening, as observed in the $Re = 10$ results shown in figure 3. Nevertheless, as the Reynolds number grows further, the lower rolls continue to shrink until they are eventually destroyed. Once $Re = 50$, all that remains is a structure reminiscent of an isothermal Poiseuille flow; this is evident in the bottom row of results

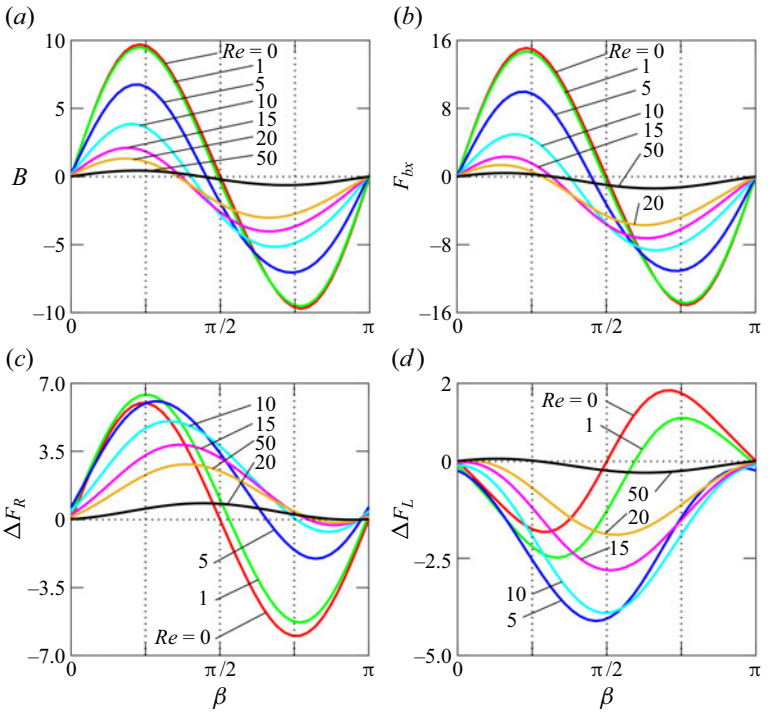


Figure 4. Flow properties as functions of the inclination angle $\beta$ when $Ra_{p,L} = 0$, $Ra_{p,R} = 500$ and $\alpha = 1$ with various Reynolds numbers in the interval $Re \in [0, 50]$. (*a*) The pressure correction $B$. (*b*) The $x$ component of the buoyancy force $F_{bx}$. Also illustrated are the heating-induced changes in the shear forces acting on the fluid at the (*c*) right (heated) wall and (*d*) left (isothermal) wall. The flow conditions when $Re = 1,\ 5,\ 10$ are marked by the vertical red lines in figure 2.

shown in figure 3. Finally, it is interesting to note that the qualitative forms of the flow topology seem to be largely independent of the inclination of the channel, and variations in $\beta$ only result in relatively minor changes in the global flow properties.

It is already well known that reducing pressure losses is possible in a horizontal channel. This phenomenon arises owing to a combination of various effects. First, reducing the direct contact between the walls and the stream lessens the frictional resistance. There is also a propulsive effect of rotation in the separation bubbles driven by horizontal density gradients. Finally, bubbles reduce the effective cross-sectional area available to the stream (Hossain *et al.* 2012; Floryan & Floryan 2015; Hossain & Floryan 2016). If the slot is inclined away from horizontal, all these effects remain operative, but now a buoyancy force acting along the channel also comes into play. The streamwise average of this additional force is zero when the channel is horizontal, but once $\beta \neq 0$, a flow-induced break in periodic symmetry generates a streamwise component (Floryan *et al.* 2022*a*,*c*, 2023*d*), which affects the pressure loss. A significant reduction in losses is feasible when $0 < \beta < \pi/2$ for which the buoyancy force assists in the flow direction while a large increase occurs for $\pi/2 < \beta < \pi$; now the buoyancy force acts against the flow direction. These cases are illustrated in figure 3. We also note in connection with figure 3 that an increase in $Re$ eliminates the separation bubbles by the stage $Re = 50$, and then the drag reduction mechanism is turned off.

The interplay between the various forces that affect the fluid motion is illustrated in figure 4. These results portray how the relative importance of the pressure gradient, the wall shear and the buoyancy forces evolve as the Reynolds number and inclination angle

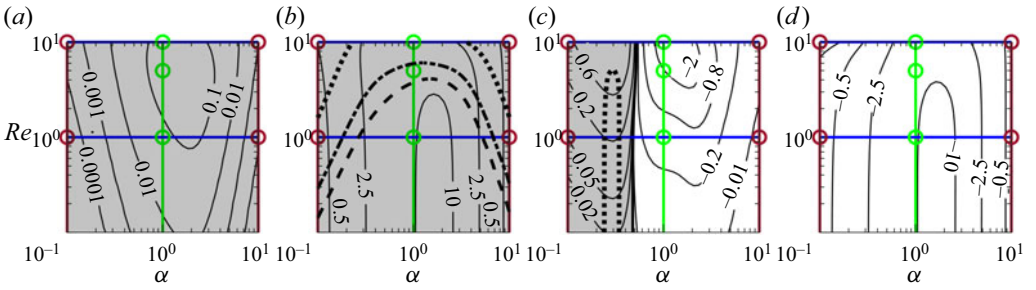


Figure 5. The pressure-gradient correction parameter $B$ as a function of $\alpha$ and $Re$ when $Ra_{p,L} = 0$ and $Ra_{p,R} = 500$. The four plots correspond to slot inclination angles $\beta =$ (*a*) 0, (*b*) $\pi/4$, (*c*) $\pi/2$ and (*d*) $3\pi/4$. The grey shading indicates those parameter combinations that lead to a reduction in the pressure loss. The thick dotted, dashed-dotted and dashed lines identify conditions leading to 10 %, 50 % and 100 % reductions in pressure losses, respectively. The green vertical lines identify the flow conditions used in figure 6, while the green circles show those in figure 3. The blue lines denote the conditions adopted in figure 7, while the brown lines and circles identify the parameter combinations used in figure 8.

vary. Figure 4(*a*) shows the cumulative effect of the three forces. This demonstrates a reduction in the pressure gradient when $\beta$ is relatively small; as $Re$ grows, the range of $\beta$ over which $B > 0$ diminishes. It is remarked that the pressure-gradient correction is not zero when the channel is horizontal (Floryan & Floryan 2015) or vertical (Floryan *et al.* 2023*d*); it is just much smaller than when the channel is inclined. The results shown in figure 4(*c*,*d*) help explain the mechanisms that underpin the heating-induced pressure-gradient reduction. Changes in the shear force on the heated wall propel fluid forward when $\beta <\sim \pi/2$ but oppose fluid movement otherwise. Interestingly, the shear force at the isothermal surface exhibits a contrasting behaviour in as much that it resists fluid movement for $\beta <\sim \pi/2$ but supports it otherwise. Typically, the magnitudes of the forces generated at the heated wall are larger. Further insight is gained from figure 4(*b*), which shows the variations in the $x$ component of the buoyancy force. It is seen that the size of this force is significantly larger than that of the shear forces, so it dominates. It must be remembered that this force cannot affect the pressure losses when the slot is horizontal since its streamwise-averaged component is precisely zero. In practice, then, for an inclined channel, it is the buoyancy mechanism that is the principal player in determining the pressure reduction, but as $\beta \to 0$ the shear forces increasingly assume this role. We also note that all the forces associated with heating seem to decrease with $Re$, as heating-induced flow modifications gradually weaken and completely disappear once the stream becomes sufficiently strong to wash out the separation bubbles.

The dependence of the pressure-gradient correction parameter $B$ on the Reynolds number $Re$ and the heating wavenumber $\alpha$ is considered in figure 5. These results demonstrate how a drag reduction is replaced by a drag increase as the inclination angle $\beta$ increases. As $\beta$ grows, the range of drag-reducing wavenumbers shrinks and moves toward long-wavelength modes, an effect we commented upon in our discussion of figure 2. We notice that when $\beta = 0$ or $\pi/4$, the most effective heating wavenumber, at least as far as drag reduction is concerned, appears to be $\alpha \approx 1$. The most significant pressure reduction occurs at longer wavelengths $\alpha \approx 0.3$ for a vertical slot, but the decrease in $B$ is also smaller. Our patterned heating no longer possesses drag-reducing properties once $\beta = 3\pi/4$. Our results thus far demonstrate that pressure-gradient losses can be significantly mitigated and, perhaps, even eliminated if a judicious combination of parameters is made.

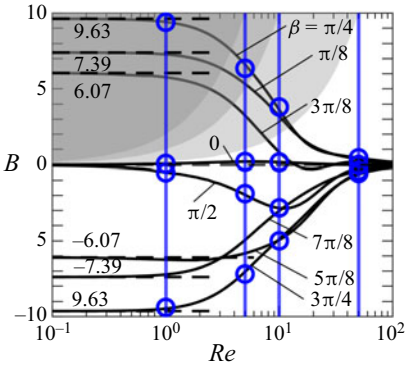


Figure 6. The pressure-gradient correction $B$ as a function of the Reynolds number $Re$ when $Ra_{p,L} = 0$, $Ra_{p,R} = 500$ and $\alpha = 1$. Plotted are the values of $B$ for the eight inclinations $\beta = j\pi/8$ with $j = 0,\ 1, \ldots,\ 7$. The flow conditions for $Re = 1,\ 5,\ 10$ are marked using blue lines in figure 2, while the circles illustrate the flow conditions used in figure 3. The various levels of grey shading indicate parameter combinations that reduce pressure losses; the borders between the shadings depict the combinations for which 10 %, 50 % or 100 % pressure-gradient reductions are possible.

Detailed information about the effects of the Reynolds number can be gleaned from the data displayed in figure 6. It is clear that the pressure-gradient correction approaches a constant, inclination-dependent limit as $Re \to 0$, corresponding to the pure natural convection that Floryan *et al.* (2022*a*) considered. Our analysis here is based on the assumption of the prescribed flow rate constraint (2.8), which, in the limit $Re \to 0$ corresponds to a zero flow rate. As heating generates a net longitudinal flow, its elimination necessitates the imposition of a pressure gradient, as suggested by figure 6. The pressure-gradient correction approaches a limit that approaches zero as $Re \to \infty$ irrespective of the inclination angle. This limit is reached when $Re$ exceeds about 100, and the separation bubbles have been completely destroyed. Furthermore, the flow loses any dependence on the heating and acquires characteristics akin to an isothermal Poiseuille flow. We emphasize that obtaining a significant reduction in pressure losses for smaller Reynolds numbers is possible.

Detailed information concerning the effects of varying the heating wavenumber can be inferred from figure 7. Heating seems to have the most marked influence on the pressure losses when $\alpha = O(1)$; naturally, the details depend on the inclination angle. The magnitude of these losses decreases in both the long- and short-heating-wavelength limits. In particular, it may be shown that $B \propto \alpha^2$ as $\alpha \to 0$ while $B \propto \alpha^{-3}$ when $\alpha \to \infty$, at least when the slot is inclined, and the details of these limits are discussed in §§ 5 and 6. Horizontal and vertical channels are somewhat special cases, as the results in figure 7 suggest. It seems that heating always reduces the pressure losses in horizontal channels irrespective of the heating wavenumber but only reduces losses in vertical channels if the wavelength is sufficiently long. There are cases of heating wavenumbers that are so effective that an opposite-signed pressure gradient must be imposed to prevent flow acceleration.

The evolution of flow structures when $\alpha = O(1)$ has already been discussed in connection with figure 3. We observed that the structures changed slightly as the inclination angle altered. To complement these findings, in figure 8, we present evidence as to the form of the flow structures in the small- and large-wavenumber limits. There is a dramatic change in the flow topology at long wavelengths as the slot is inclined at an angle increasing from horizontal. The long-wavelength structures can be analysed, and

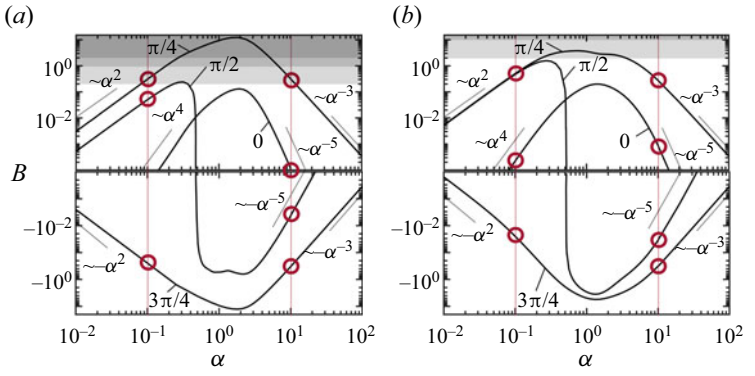


Figure 7. The pressure-gradient correction $B$ when $Ra_{p,L} = 0$ and $Ra_{p,R} = 500$ for the four channel inclinations $\beta = j\pi/4$ with $j = 0, 1, 2, 3$. Shown are the results for two Reynolds numbers: (*a*) $Re = 1$ and (*b*) $Re = 10$. The flow conditions used in this figure are shown using blue lines in figure 5. The various degrees of grey shading indicate those parameter combinations that reduce the pressure losses; the borders between the different shadings correspond to 10 %, 50 % and 100 % pressure-gradient reduction. The circles identify the conditions adopted in figure 8.

the pertinent results are summarized in § 5. There, we point out that the limit $\beta \to 0$ is a special case, and this conclusion is supported by the flow structures displayed in the first column of rows 1 and 3 of figure 8. On the other hand, at short wavelengths, boundary layers form near the heated walls. The asymptotic solutions described in § 6 show that the details of the boundary layers differ if the channel is horizontal or vertical, but the modifications are somewhat technical so that the overall flow topology does not change significantly.

One last aspect of the problem that warrants attention is the effect of the heating intensity. The change in the pressure gradient is proportional to $Ra_{p,R}^2$ for relatively weak heating; this result is evident in the results contained in figure 9. In the opposite case of intense heating, we have evidence of saturation, and the magnitude of $B$ does not grow indefinitely as $Ra_{p,R}$ increases, at least in the case of small Reynolds numbers (see figure 9*a*). We see that the case of a vertical channel is somewhat a special case in as much that there is a transition from a reduction to a growth in the pressure losses, which occurs at $Ra_{p,R} \approx 400$ (Floryan *et al.* 2023*d*). At larger Reynolds numbers, the behaviour is rather more intricate. Now, a switch between reduced and enhanced pressure-gradient losses is possible in slots that no longer need to be vertical.

One may inquire about the stability properties of these flows and whether a transition to secondary states might occur. Previous work on analysing flows in horizontal channels has shown that the periodic Rayleigh number must reach values in excess of 2500 for any instability to appear, irrespective of the heating wavenumber (Hossain & Floryan 2013*b*, 2015*b*). The results summarized in figure 9 demonstrate a saturation effect associated with an increase in heating intensity above $Ra_{p,R} = 2000$. The upshot is that such large intensities are of little interest in developing practical drag-reducing techniques. Strictly, one should check whether the intensity of the critical heating decreases as the inclination angle increases. However, since the channel-transverse component of the buoyancy force drives convective instabilities, and this component drops as the inclination angle grows, so the critical heating intensity is expected to increase with the inclination angle.

The above analysis raises a natural question about the energy costs of reducing pressure losses. The reduction of energy delivered through the pressure gradient (per unit length) is $\Delta E_{pres} = \frac{4}{3}ReB$ with variations of $B$ given in figure 2. The heat energy delivered to

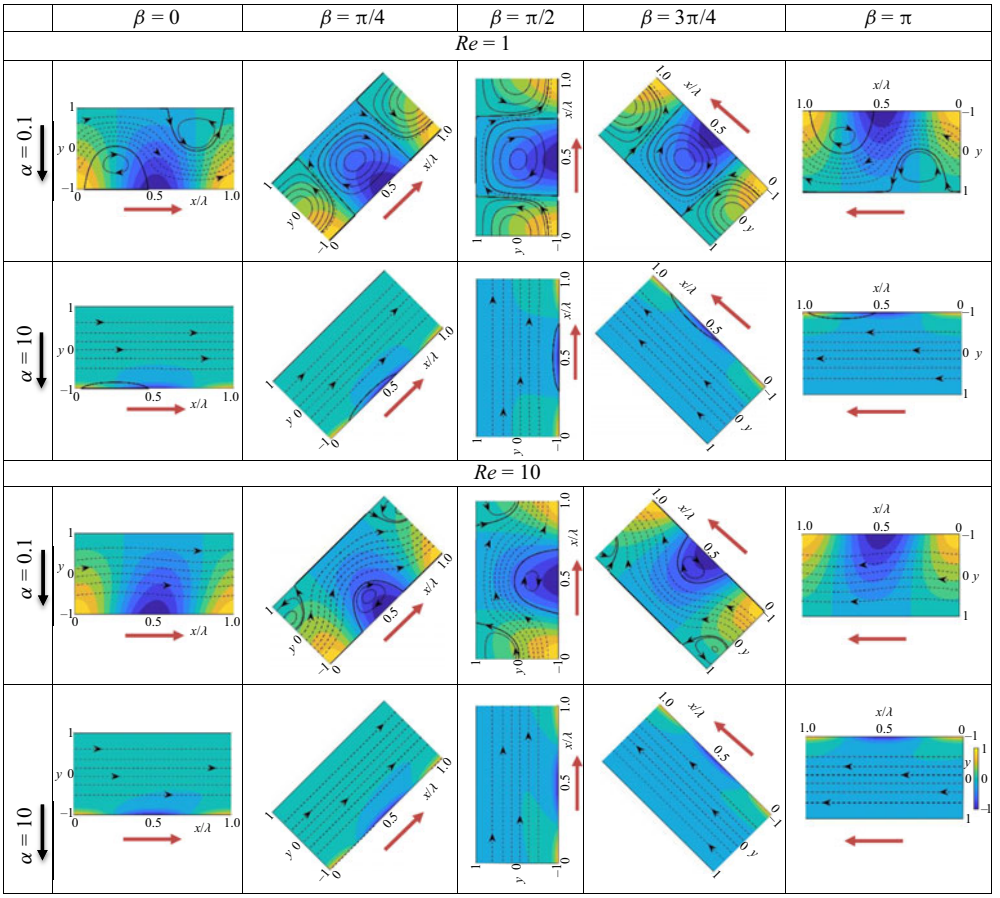


Figure 8. The flow and temperature fields for flows with heating intensities $Ra_{p,L} = 0$ and $Ra_{p,R} = 500$. Shown are the structures that correspond to relatively long-wavelength ($\alpha = 0.1$) and short-wavelength ($\alpha = 10$) modes and at the two Reynolds numbers $Re = 1$ and $Re = 10$. The background colour illustrates the temperature field. The black arrows show the direction of gravity force, while the red arrows denote the direction of pressure-gradient force. The flow conditions used in these plots are marked in figures 5 and 7. In all the plots the temperature has been normalized with its maximum $\theta_{max}$.

the system has two parts. The first one involves heat flow between the walls quantified by the average Nusselt number $Nu_{av}$, and it represents the true energy cost. The second one represents the energy flow between the hot and cold sections of the wall. This heat flow averages out to zero over a wavelength, but there must be a cost associated with maintaining temperature variations along the wall. Some information about it is provided by evaluating heat flow leaving/entering the wall per half-wavelength, which is quantified by the horizontal Nusselt number $Nu_{h,R}$. Variations of $Nu_{av}$ and $Nu_{h,R}$ for the same conditions as in figure 2 are displayed in figure 10. While $Nu_{h,R}$ exceeds by an order of magnitude $Nu_{av}$, as noted in Hossain & Floryan (2013*a*), it is not a good measure of energy cost as this heat is recovered over the next half of the heating wavelength, i.e. it averages out to zero. The actual energy cost of maintaining temperature variations along the wall is a function of the details of the construction of the heating system and cannot be determined unless the wall composition is specified and conduction within the wall is accounted for. This cost is expected to be much smaller than the heat flow over

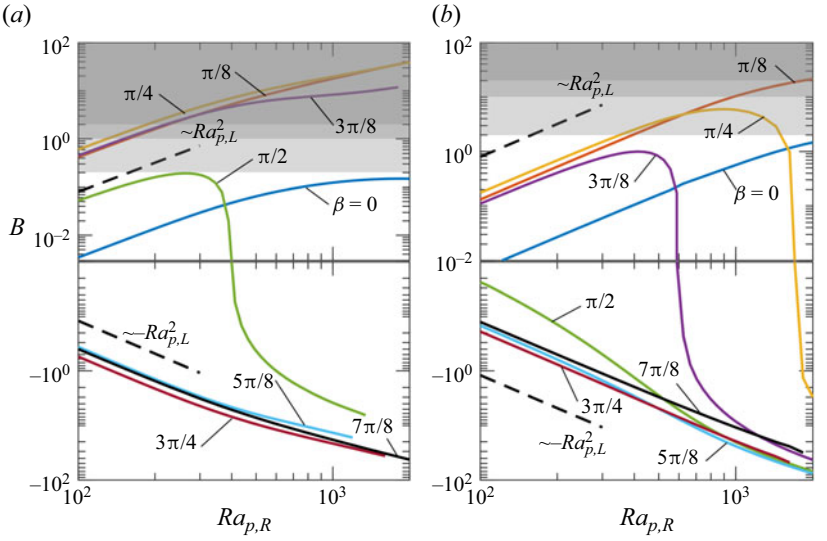


Figure 9. The pressure-gradient correction $B$ for a heating wavenumber $\alpha = 1$ and eight inclination angles $\beta = j\pi/8$ for $j = 0,\ 1,\ \ldots,\ 7$. Two Reynolds numbers are considered: (*a*) $Re = 1$ and (*b*) $Re = 10$. The different levels of shading indicate parameter combinations that reduce pressure losses, and the borders between the colours correspond to cases of 10 %, 50 % and 100 % pressure-gradient reduction.

half a wavelength. The magnitude of energy fluxes can be estimated based on the data from figures 2 and 10. Consider $Re = 5$ (the middle columns in these figures) and take the middle of the drag-reducing zone, which gives $B \approx 5$. The energy saving due to the reduction of pressure losses is ∼33, the energy cost due to the heat flow between the walls is ∼20 and the amount of energy leaving the wall and re-entering it is ∼300. This underlines that wall construction dominates the energy cost, but an analysis of possible wall constructions and their energy efficiencies is outside the scope of our analysis. If this energy cost can be eliminated, or at least significantly reduced, it might be possible to develop a system where energy cost of loss reduction is smaller than the energy saved by loss reduction. It should be remarked that the cost could be acceptable even if energy cost of reduction significantly exceeds the reduction itself as one may be able to use waste energy as a heating source, making the energy cost largely immaterial.

## 4. Heating applied to both sides of the channel

We now briefly discuss the situations that can arise when both sides of the slot are heated. Our observations so far suggest that changes in the friction at the heated wall are larger than at the isothermal wall, thereby reducing pressure losses. When both walls are heated, the reduction of losses is expected to be enhanced as the separation bubbles on both walls are directly driven by the heating applied at each. This additional heating introduces two further parameters into the problem: the intensity of the heating of the second surface and the phase difference $\Omega$ between the two patterns. An in-depth study of all possible parameter combinations would lead to an unwieldy plethora of results. To focus matters, we concentrate on understanding the role played by the phase difference when equal heating is applied to the two walls so $Ra_{p,L} = Ra_{p,R}$. Calculations show that the details of the pressure losses depend strongly on the phase $\Omega$ and the channel orientation $\beta$, and some sample results are illustrated in figure 11. The value of the correction $B$ seems to

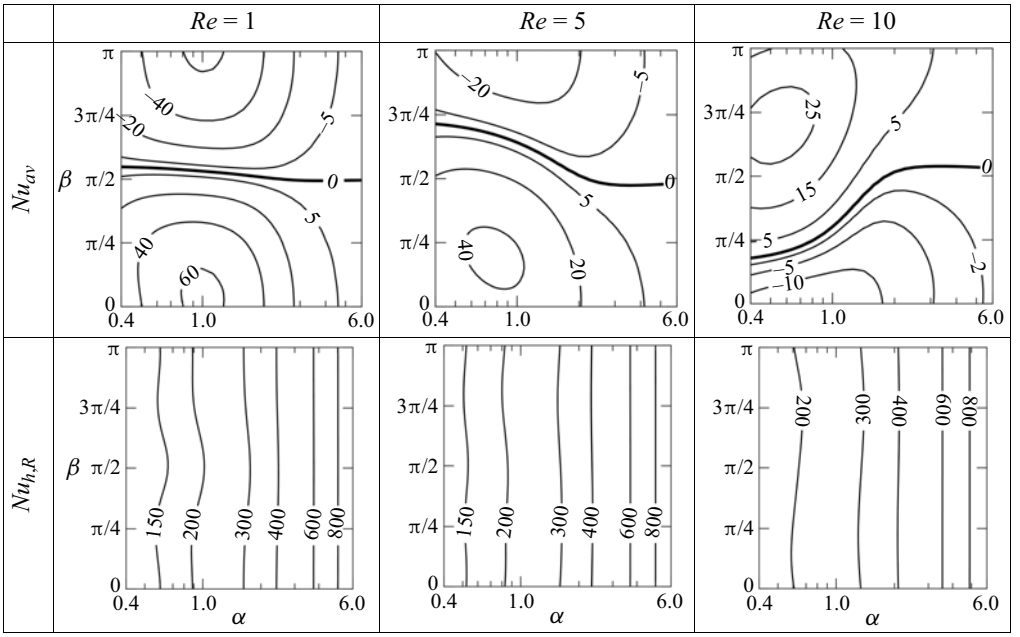


Figure 10. The variations of the average Nusselt number $Nu_{av}$ and the horizontal Nusselt number $Nu_{h,R}$ (see (2.10)) as functions of the heating wavenumber $\alpha$ and the slot inclination angle $\beta$ when only the right wall is heated with $Ra_{p,R} = 500$.

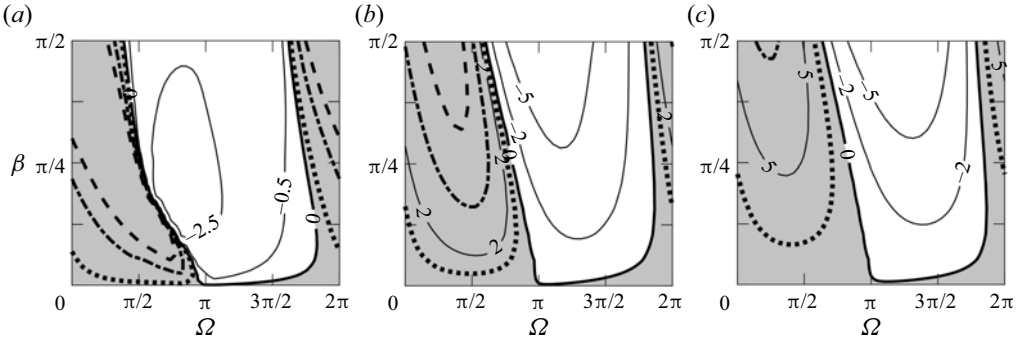


Figure 11. The pressure-gradient correction $B$ as a function of $\Omega$ and $\beta$ when $Ra_{p,L} = Ra_{p,R} = 500$ and $\alpha = 1$. The three plots correspond to a Reynolds number $Re =$ (*a*) 1, (*b*) 5 and (*c*) 10. The shading indicates those parameter combinations that lead to a reduction in pressure losses. The thick dotted, dashed-dotted and dashed lines identify the conditions leading to 10 %, 50 % and 100 % reduction of pressure losses.

depend only weakly on the phase $\Omega$ when the channel is horizontal. This behaviour is perhaps illusory, as there is some variation with $\Omega$, which is largely hidden on the scale used to plot figure 11. Hossain & Floryan (2016) discuss this problem in some detail. It is recalled that the streamwise component of the mean buoyancy force is zero when the slot is horizontal, but this no longer holds once the channel is inclined. This induces much larger changes in the value of $B$ and, as the offset $\Omega$ is adjusted, significant swings in the magnitude of $B$ arise and, moreover, it can change sign.

A better understanding of possible flow responses can be gained from the data displayed in figure 12. Here, we consider the quantity $B_{comp} = (B_2 - B_1)/B_1$ which gives a very

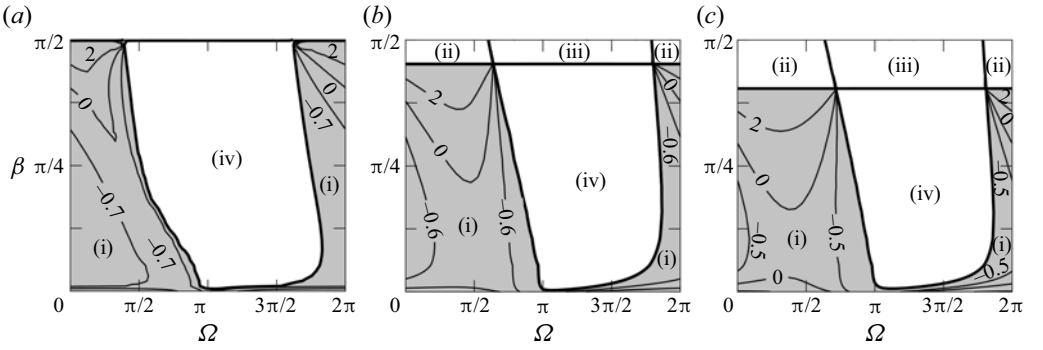


Figure 12. A comparison of the effectiveness of the one-wall and two-wall heating as functions of $\Omega$ and $\beta$ when $Ra_{p,L} = Ra_{p,R} = 500$ and $\alpha = 1$ for Reynolds numbers $Re =$ (*a*) 1, (*b*) 5 and (*c*) 10. Shown plotted is the quantity $B_{comp} = (B_2 - B_1)/B_1$ in which $B_j$ denotes the pressure-gradient correction observed when $j$ walls are heated ($j = 1, 2$). The parameter space is divided into four regions (i)–(iv) as defined in the text.

rough estimate of the comparison of the system performance, whether only one wall or both walls are heated. In this definition, we denote by $B_j$ the pressure-gradient correction observed when $j$ walls are heated ($j = 1, 2$). This then naturally leads to a division of the parameter space into four regions (i)–(iv) defined by (i) $B_1 > 0,\ B_2 > 0$; (ii) $B_1 < 0,\ B_2 > 0$; (iii) $B_1 < 0,\ B_2 < 0$; and (iv) $B_1 > 0,\ B_2 < 0$. We have conditions for improved pressure corrections with two-wall heating. It seems that within (ii), there is also an advantage in using two-wall heating as it generates a positive pressure-gradient correction, while the same conditions give a negative pressure-gradient correction for one-wall heating. Overall, the advantage of the two-wall heating seems to increase with $Re$.

In the next two sections, we analytically examine the cases of long-wavelength and short-wavelength heating. This serves twin objectives: on the one hand, they provide insight into the mechanisms that underpin the flow structure; on the other hand, comparison with the numerical simulations in appropriate limits gives us additional confidence in the accuracy of the calculations.

## 5. Long-wavelength heating

We begin a discussion of the analytic solution for the flow by considering long-wavelength heating ($\alpha \ll 1$). To that end, we introduce the stretched coordinate $X = \alpha x$, which brings the governing equations and thermal boundary conditions to the following form:

$$\alpha[Re(1-y^2) + u_1]u_{1X} + v_1(-2Re\, y + u_{1y}) = -\alpha p_{1X} + \alpha^2 u_{1XX} + u_{1yy} + \frac{\theta_1}{Pr}\sin\beta, \tag{5.1a}$$

$$\alpha[Re(1-y^2) + u_1]v_{1X} + v_1 v_{1y} = -p_{1y} + \alpha^2 v_{1XX} + v_{1yy} + \frac{\theta_1}{Pr}\cos\beta, \tag{5.1b}$$

$$\alpha[Re(1-y^2) + u_1]\theta_{1X} + v_1\theta_{1y} = \frac{1}{Pr}(\alpha^2\theta_{1XX} + \theta_{1yy}), \tag{5.1c}$$

$$\alpha u_{1X} + v_{1y} = 0, \tag{5.1d}$$

with the thermal boundary conditions becoming

$$\theta_1(X, -1) = \tfrac{1}{2}Ra_{p,R}\cos X, \quad \theta_1(X, 1) = \tfrac{1}{2}Ra_{p,L}\cos(X + \Omega). \tag{5.2a,b}$$

Notice that we have incorporated the phase shift in the heating profiles and allowed different magnitudes of heating at the two walls. It is helpful for the subsequent calculations to define the three related quantities

$$R_1 = Ra_{p,R} + Ra_{p,L}\cos\Omega, \quad R_2 = Ra_{p,R} - Ra_{p,L}\cos\Omega \quad \text{and} \quad R_3 = Ra_{p,L}\sin\Omega. \tag{5.3a–c}$$

We seek solutions that assume the structure

$$(u_1, v_1, p_1, \theta_1) = \alpha^{-1}(0, 0, \hat{P}_{-1}, 0) + (\hat{U}_0, 0, \hat{P}_0, \hat{\theta}_0) + \alpha(\hat{U}_1, \hat{V}_0, \hat{P}_1, \hat{\theta}_1) + \alpha^2(\hat{U}_2, \hat{V}_1, \hat{P}_2, \hat{\theta}_2) + \cdots, \tag{5.4}$$

where all the unknowns are functions of $X$ and $y$. Given the form of the boundary conditions, we are led to the leading-order solutions

$$\hat{U}_0 = -\frac{1}{24Pr}y(1-y^2)(R_2\cos X + R_3\sin X)\sin\beta, \quad \hat{V}_0 = -\frac{1}{96Pr}(1-y^2)^2(R_3\cos X - R_2\sin X)\sin\beta, \tag{5.5a,b}$$

$$\hat{\theta}_0 = \frac{1}{4}[(R_1 - R_2 y)\cos X - R_3(1+y)\sin X] \quad \text{and} \quad \hat{P}_{-1} = \frac{1}{4Pr}(R_1\sin X + R_3\cos X)\sin\beta. \tag{5.5c,d}$$

At $O(\alpha)$ the thermal field consists of mean and $X$-dependent parts. It may be shown that

$$\hat{\theta}_1(X, y) = -\tfrac{1}{4}PrRe[F_1(y)\sin X + F_2(y)\cos X] + \tfrac{1}{384}[F_3(y)\sin 2X + F_4(y)\cos 2X + F_5(y)]\sin\beta, \tag{5.6}$$

where the polynomials $F_1(y)$–$F_5(y)$ are defined to be

$$F_1(y) = \tfrac{1}{60}(1-y^2)[5(y^2-5)R_1 - y(3y^2-7)R_2], \tag{5.7a}$$

$$F_2(y) = \tfrac{1}{60}R_3(1-y^2)(3y^3+5y^2-7y-25), \tag{5.7b}$$

$$F_3(y) = \tfrac{1}{60}(1-y^2)(3y^4-2y^2-17)(R_3^2-R_2^2) - \tfrac{1}{30}y(1-y^2)(7-3y^2)(R_3^2+R_1R_2), \tag{5.7c}$$

$$F_4(y) = \tfrac{1}{30}(1-y^2)(3y^4+3y^3-2y^2-7y-17)R_2R_3 - \tfrac{1}{30}y(1-y^2)(3y^2-7)R_1R_3, \tag{5.7d}$$

$$F_5(y) = -\tfrac{1}{30}y(1-y^2)(7-3y^2)(R_1+R_2)R_3. \tag{5.7e}$$

The remaining quantities satisfy the equations

$$\hat{U}_{1yy} - \hat{P}_{0X} + \frac{1}{Pr}\hat{\theta}_1\sin\beta = Re(1-y^2)\hat{U}_{0X} - 2Rey\hat{V}_0 + \hat{U}_0\hat{U}_{0X} + \hat{V}_0\hat{U}_{0y}, \tag{5.8a}$$

$$\hat{P}_{0y} = \frac{1}{Pr}\hat{\theta}_0\cos\beta \quad \text{and} \quad \hat{U}_{1X} + \hat{V}_{1y} = 0. \tag{5.8b,c}$$

Strictly, we only need to ascertain the parts of the solutions proportional to $\sin X$ and $\cos X$; the nonlinear terms in (5.8*a*) will generate terms proportional to $\sin 2X$ and $\cos 2X$ but these do not contribute to calculating the orders that must be considered. It then follows

that the relevant parts of the solution of (5.8) are

$$\hat{U}_1(X,y) = \frac{1}{10\,080}ReR_3\left(F_6 - \frac{F_7}{Pr}\right)\cos X\sin\beta \; + \frac{1}{10\,080}Re\;\left(F_8 + R_2\frac{F_7}{Pr}\right)\sin X\sin\beta$$
$$+ \frac{1}{480Pr}(1-y^2)[R_3(5y^2-20y+1)\cos X + (R_2(1-5y^2)$$
$$+ 20R_1y)\sin X]\cos\beta + U_{M1}(y) + \cdots, \tag{5.9a}$$

$$\hat{V}_1(X,y) = \frac{1}{10\,080}ReR_3\left(F_9 - \frac{F_{10}}{Pr}\right)\sin X\sin\beta + \frac{1}{10\,080}Re\left(F_{11} - R_2\frac{F_{10}}{Pr}\right)\cos X\sin\beta$$
$$- \frac{1}{480Pr}(1-y^2)^2[R_3(y+5)\sin X - (5R_1 - R_2y)\cos\;X]\cos\beta + \cdots, \tag{5.9b}$$

$$\hat{P}_0 = \frac{17}{210}Re(R_3\sin X - \;R_1\cos X)\sin\beta$$
$$+ \frac{1}{40Pr}[(R_2(1-5y^2) + 10R_1y)\cos X - R_3(5y^2+10y-1)\sin X]\cos\beta + \cdots, \tag{5.9c}$$

in which the polynomials $F_6(y)$–$F_{11}(y)$ are given by

$$F_6(y) = (1-y^2)(3y^5 + 7y^4 - 18y^3 - 98y^2 + 31y + 19), \tag{5.10a}$$
$$F_7(y) = y(y^2-1)(5y^4 - 16y^2 + 19), \tag{5.10b}$$
$$F_8(y) = (y^2-1)[(3y^5 - 18y^3 + 31y)R_2 - (7y^4 - 98y^2 + 19)R_1], \tag{5.10c}$$
$$F_9(y) = -\tfrac{1}{8}(y^2-1)^2(3y^4 + 8y^3 - 22y^2 - 152y + 51), \tag{5.10d}$$
$$F_{10}(y) = \tfrac{1}{8}(y^2-1)^2(5y^4 - 18y^2 + 29), \tag{5.10e}$$
$$F_{11}(y) = -\tfrac{1}{8}(y^2-1)^2[(3y^4 - 22y^2 + 51)R_2 - 8y(y^2-19)R_1]. \tag{5.10f}$$

Furthermore, the mean part of the streamwise velocity $\hat{U}_{M1}(y)$ is another polynomial, but this consists only of terms of odd degree, so the mass flux across the slot $-1 \le y \le 1$ is zero.

We now move on to consideration of the $O(\alpha^2)$ terms. If we suppose that the pressure gradient

$$p_X = A\alpha^2 + \cdots, \tag{5.11}$$

then the $O(\alpha^2)$ terms in the streamwise momentum and energy equations are

$$Re(1-y^2)\hat{U}_{1X} - 2Rey\hat{V}_1 + \hat{U}_0\hat{U}_{1X} + \hat{U}_1\hat{U}_{0X} + \hat{V}_0\hat{U}_{1y} + \hat{V}_1\hat{U}_{0y} = -(A+\cdots) + \hat{U}_{0XX} + \hat{U}_{2yy} + \frac{1}{Pr}\hat{\theta}_2\sin\beta, \tag{5.12a}$$

$$Re(1-y^2)\hat{\theta}_{1X} + \hat{U}_0\hat{\theta}_{1X} + \hat{U}_1\hat{\theta}_{0X} + \hat{V}_0\hat{\theta}_{1y} + \hat{V}_1\hat{\theta}_{0y} = \frac{1}{Pr}(\hat{\theta}_{0XX} + \hat{\theta}_{2yy}). \tag{5.12b}$$

If we denote the mean part of $\hat{\theta}_2(x,y)$ by $\hat{\theta}_{2M}(y)$ then (5.12*b*) furnishes an expression for $(\hat{\theta}_{2M})_{yy}$ that can be integrated twice, subject to the requirement that $\hat{\theta}_{2M}$ vanishes at $y = \pm 1$. This result is substituted into (5.12*a*) for the mean function $\hat{U}_{2M}(y)$ which can be

found subject to $\hat{U}_{2M}(\pm 1) = 0$; the pressure gradient is then adjusted to ensure the mean mass flux is zero. After some algebraic manipulation and simplification, we find that

$$\begin{aligned} A = {} & \frac{1}{12\,600\ Pr}(Ra_{p,R}^2 - Ra_{p,L}^2)\sin 2\beta + \frac{\sin^2\beta}{227\,026\,800 Pr^2} Re \\ & \times \{(Ra_{p,L}^2 + Ra_{p,R}^2 - 2Ra_{p,L}\ Ra_{p,R}\cos\Omega)(51 - 790\ Pr) \\ & + [5876(Ra_{p,L}^2 + Ra_{p,R}^2) + 9620\ Ra_{p,L} Ra_{p,R}\cos\Omega]Pr^2\}, \end{aligned} \tag{5.13}$$

and the associated pressure gradient is $B = A\alpha^2$.

The reader may note that when heating is applied at the right wall only, the above expression simplifies to the form

$$\alpha^2 \left\{ \frac{1}{227\,026\,800 Pr^2} Re\, Ra_{p,R}^2 (51 - 790Pr + 5876Pr^2)\sin^2\beta + \frac{1}{12\,600\ Pr} Ra_{p,R}^2 \sin 2\beta \right\}. \tag{5.14}$$

The first term is always positive for any $Pr$ while the second term becomes negative for $\beta \in (\pi/2, \pi)$ and for $\beta \in (3\pi/2, 2\pi)$ with precise boundaries of these intervals being discussed later in the presentation. It is noted that a vertical ($\beta = \pi/2$) has the flow moving upwards. This wall begins to serve as the upper wall with a further increase of $\beta$ with the flow directed to the left. It becomes horizontal when $\beta = \pi$, with the flow then moving to the left and the upper wall being heated. A further increase of $\beta$ results in the flow travelling downwards with the upper wall now heated. It becomes vertical at $\beta = 3\pi/2$ with the flow now downward and the left wall heated. The channel returns to a horizontal position at $\beta = 2\pi$, with the lower wall being heated and the flow moving to the right. Reduction of pressure losses is possible only for the channel orientation between vertical with the right wall heated and being horizontal with the upper wall heated and between being vertical with the left wall heated and horizontal with the lower wall heated. The above equation also shows that the solution for the inclined channel in the limit of $\beta \to 0$ (horizontal channel) has a different structure with $A = 0(\alpha^4)$ (Floryan & Floryan 2015) rather than $A = 0(\alpha^2)$ for the inclined channel. Details of this transition are omitted from this discussion.

We can also comment on the Nusselt number form. If we take the expression for $\hat{\theta}_{2M}$ and evaluate the derivative at $y = -1$ we find that

$$\begin{aligned} \left.\frac{\mathrm{d}\hat{\theta}_{2M}}{\mathrm{d}y}\right|_{y=-1} = {} & \frac{1}{45\,360} Re(Ra_{p,R}^2 - Ra_{p,L}^2)(1 - 10Pr)\sin\beta - \frac{1}{12\,600}(9Ra_{p,R}^2 + 9Ra_{p,L}^2 \\ & + 17Ra_{p,L}Ra_{p,R}\cos\Omega)\cos\beta. \end{aligned} \tag{5.15}$$

Figure 13 compares the asymptotic predictions against some numerical simulations of the complete governing system. We plot the form of $B = A\alpha^2$ as given by (5.13) and the Nusselt number $Nu_{av}$ predicted by (5.15). The comparison shows excellent agreement between the analytical and numerical findings, at least for wavenumbers $\alpha < 0.1$.

## 6. Short-wavelength heating

Here, we consider the opposite limit of short-wavelength heating. When $\alpha$ is large, most of the interesting motion occurs near the edges of the channel, so let us consider appropriate

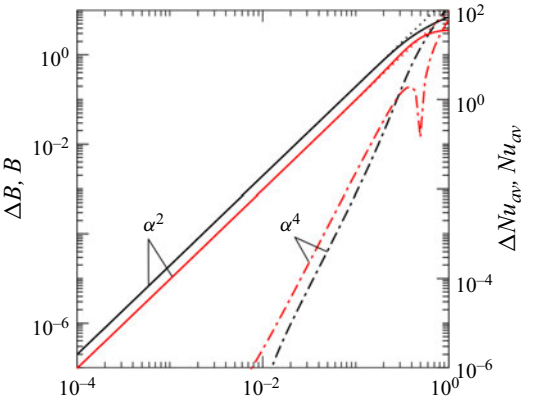


Figure 13. Variations of the numerically determined ($B_n$, solid black line) and the analytically determined ($B_a$, dotted black line) pressure-gradient corrections, and of the numerically determined ($Nu_{av,n}$ solid red line) and the analytically determined ($Nu_{av,a}$, dotted red line) average Nusselt numbers as functions of the heating wavenumber $\alpha$ as $\alpha \to 0$ for $Re = 1$, $Ra_{p,R} = 400$, $Ra_{p,L} = 0$. The dashed-dotted lines identify the differences $\Delta B = |B_a - B_n|$ (black line) and $\Delta Nu = |Nu_{av,n} - Nu_{av,a}|$ (red line). These results suggest that the leading-order solutions are indeed in error by $O(\alpha^4)$.

scales so that $X = \alpha x$ and $Y = \alpha(y + 1)$ near the right-hand wall. The governing equations written in these scales become

$$\alpha^{-1}[Re(2\alpha Y - Y^2) + \alpha^2 u_1]u_{1X} + \alpha^{-1} v_1[2Re(\alpha - Y) + \alpha^2\, u_{1Y}]$$
$$= -\alpha p_{1X} + \alpha^2(u_{1XX} + u_{1YY}) + Pr^{-1}\theta_1 \sin\beta, \tag{6.1a}$$

$$\alpha^{-1}[Re(2\alpha Y - Y^2) + \alpha^2 u_1]v_{1X} + \alpha\; v_1 v_{1Y} = -\alpha\; p_{1Y} + \alpha^2(v_{1XX} + v_{1YY}) + Pr^{-1}\theta_1 \cos\beta, \tag{6.1b}$$

$$u_{1X} + v_{1Y} = 0, \tag{6.1c}$$

$$\alpha^{-1}[Re(2\alpha Y - Y^2) + \alpha^2 u_1]\theta_{1X} + \alpha\; v_1\theta_{1Y} = \alpha^2 Pr^{-1}(\theta_{1XX} + \theta_{1YY}), \tag{6.1d}$$

where the subscript 1 refers to flow modulations caused by the heating. We solve these equations subject to periodic heating on the edges of the slot so that

$$\theta_1(X, -1) = \tfrac{1}{2}Ra_{p,R}\cos X, \qquad \theta_1(X, 1) = \tfrac{1}{2}Ra_{p,L}\cos(X + \Omega). \tag{6.2}$$

When $\alpha \,''1$ we seek solutions that assume the structure

$$u_1 = \alpha^{-2}\left(\sum_0^\infty \alpha^{-j}\hat{U}_j\right), \quad v_1 = \alpha^{-2}\left(\sum_0^\infty \alpha^{-j}\hat{V}_j\right), \quad p_1 = \alpha^{-1}\left(\sum_0^\infty \alpha^{-j}\hat{P}_j\right), \quad \theta_1 = \left(\sum_0^\infty \alpha^{-j}\hat{\Theta}_j\right), \tag{6.3}$$

where all the unknowns are functions of $X$ and $Y$. Leading-order terms in the thermal equation give

$$\hat{\Theta}_{0XX} + \hat{\Theta}_{0YY} = 0 \quad \Rightarrow \quad \hat{\Theta}_0(X, Y) = \tfrac{1}{2}Ra_{p,R}\;\exp(-Y)\cos X, \tag{6.4}$$

to satisfy the boundary condition on $Y = 0$ and to decay as $Y \to \infty$. Next-order equations show that $\hat{\Theta}_1(X, Y) \equiv 0$; we also have $\hat{U}_1 = \hat{V}_1 = \hat{P}_1 \equiv 0$. At $O(\alpha^{-2})$ we find that

$$2Y\, Re\hat{\Theta}_{0X} = Pr^{-1}(\hat{\Theta}_{2XX} + \hat{\Theta}_{2YY}) \quad \Rightarrow \quad \hat{\Theta}_2(X, Y) = \tfrac{1}{4}PrReRa_{p,R}Y(Y + 1)exp(-Y)\sin X, \tag{6.5}$$

while the $O(1)$ terms in the two momentum and continuity equations give

$$0 = -\hat{P}_{0X} + \hat{U}_{0XX} + \hat{U}_{0YY} + Pr^{-1}\hat{\Theta}_0 \sin\beta, \quad 0 = -\hat{P}_{0Y} + \hat{V}_{0XX} + \hat{V}_{0YY} + \overline{\mathrm{Pr}}^{-1}\hat{\Theta}_0 \cos\beta, \quad \hat{U}_{0X} + \hat{V}_{0Y} = 0, \tag{6.6a–c}$$

whose solution is

$$\hat{U}_0 = -\frac{Ra_{p,R}}{16Pr} Y(2-Y)exp(-Y)\sin(X-\beta), \quad \hat{V}_0 = \frac{Ra_{p,R}}{16Pr} Y^2 exp(-Y)\cos(X-\beta), \tag{6.7a,b}$$

$$\hat{P}_0 = \frac{Ra_{p,R}}{8Pr}[(2Y+3)\cos X\cos\beta + (2Y+1)\sin X\sin\beta]. \tag{6.7c}$$

We next move back to the energy equation at $O(\alpha^{-3})$. We have

$$\hat{U}_0\ \hat{\Theta}_{0X} + \hat{V}_0\hat{\Theta}_{0Y} - Re\ Y^2\hat{\Theta}_{0X} = \frac{1}{Pr}(\hat{\Theta}_{3XX} + \hat{\Theta}_{3YY}), \tag{6.8}$$

which, on substituting the leading-order results, becomes

$$\begin{aligned}\hat{\Theta}_{3XX} + \hat{\Theta}_{3YY} = {} & \tfrac{1}{32}Ra_{p,R}^2 Y[(1-Y)\cos\beta - \cos(2X-\beta)]\exp(-2Y) \\ & + \tfrac{1}{2}PrReRa_{p,R}Y^2\exp(-Y)\sin X.\end{aligned} \tag{6.9}$$

This equation admits the solution

$$\begin{aligned}\hat{\Theta}_3(X,Y) = {} & -\tfrac{1}{24}PrReRa_{p,R}Y(2Y^2+3Y+3)\ exp(-Y)\sin X \\ & + \tfrac{1}{512}Ra_{p,R}^2 Y(1+2Y)exp(-2Y)\cos(2X-\beta) \\ & + \tfrac{1}{256}Ra_{p,R}^2[1-(1+2Y+2Y^2)exp(-2Y)]\cos\beta.\end{aligned} \tag{6.10}$$

The streamwise momentum equation at $O(\alpha^{-5})$ gives

$$-Y^2Re\hat{U}_{0X} + \hat{U}_0\hat{U}_{0X} - 2YRe\hat{V}_0 + \hat{V}_0\hat{U}_{0Y} = -\hat{P}_{3X} + \hat{U}_{3XX} + \hat{U}_{3YY} + \frac{\hat{\Theta}_5}{Pr}\sin\beta. \tag{6.11}$$

Again, we are interested in the mean parts of this equation. If we suppose that $\hat{P}_{3M} = AX$ then the mean part of $\hat{U}_3$, call it $\hat{U}_{3M}(y)$, satisfies

$$\cdots = -\boldsymbol{A} + \hat{\boldsymbol{U}}''_{3M} + \frac{1}{\boldsymbol{Pr}}\hat{\boldsymbol{\Theta}}_{3M}\sin\boldsymbol{\beta}. \tag{6.12}$$

We do not need to solve this explicitly, for it is sufficient to note that for large $Y$ we have

$$\hat{U}''_{3M} \sim \left[A - \frac{Ra_{p,R}^2}{512Pr}\sin 2\beta\right] \Rightarrow \hat{U}_{3M} \sim \left[A - \frac{Ra_{p,R}^2}{512Pr}\sin 2\beta\right]\frac{1}{2}Y^2. \tag{6.13}$$

We point out that all the terms on the left-hand side of (6.12) decay exponentially for large $Y$, so they cannot contribute to the leading-order form of the mean flow solution at large values.

This step completes the analysis of the wall layer. We see that the $O(\alpha^{-3})$ component of $\theta_1$ tends to a constant as $Y \to \infty$ (see (6.10)) while the $O(\alpha^{-5})$ component $\hat{U}_{3M}(y)$ grows

quadratically. Then, across the bulk of the slot where $y = O(1)$, we have that

$$u_1 = \alpha^{-3}\tilde{U}(y) + \cdots, \quad \theta_1 = \alpha^{-3}\tilde{\Theta}(y) + \cdots, \quad p_1 = \alpha^{-3}Ax + \cdots, \tag{6.14a–c}$$

and these satisfy

$$0 = -A + \frac{\mathrm{d}^2\tilde{U}}{\mathrm{d}y^2} + \frac{1}{Pr}\tilde{\Theta}\sin\beta, \quad \frac{\mathrm{d}^2\tilde{\Theta}}{\mathrm{d}y^2} = 0. \tag{6.15}$$

The form of (6.10) shows that for matching, we require

$$\tilde{\Theta} \to \frac{Ra_{p,R}^2}{256}\cos\beta \quad \text{as } y \to -1. \tag{6.16}$$

An exactly parallel calculation at the left wall shows that we must also demand

$$\tilde{\Theta} \to -\frac{Ra_{p,L}^2}{256}\cos\beta \quad \text{as } y \to 1. \tag{6.17}$$

Hence,

$$\tilde{\Theta}(y) = \tfrac{1}{512}[Ra_{p,R}^2 - Ra_{p,L}^2 - (Ra_{p,L}^2 + Ra_{p,R}^2)y]\cos\beta, \tag{6.18}$$

so that

$$\frac{\mathrm{d}^2\tilde{U}}{\mathrm{d}y^2} = A - \frac{1}{1024\,Pr}[Ra_{p,R}^2 - Ra_{p,L}^2 - (Ra_{p,L}^2 + Ra_{p,R}^2)y]\sin 2\beta. \tag{6.19}$$

There is no need to solve this completely – if we integrate twice and impose that $\tilde{U}(\pm 1) = 0$, this requires that the constant term in the above equation disappears. Hence,

$$A = \frac{1}{1024\,Pr}(Ra_{p,R}^2 - Ra_{p,L}^2)\sin 2\beta. \tag{6.20}$$

In conclusion, we see that to maintain a constant mass flux through the channel, we need to impose a pressure-gradient correction $B = \alpha^{-3}A$, where $A$ is given by (6.20). This correction does not depend on $Re$ at the leading order of approximation. If only the right wall is heated, a reduction of pressure losses can be achieved only for $\beta \in (0, \pi/2)$ or for $\beta \in (\pi, 3\pi/2)$. The reader may note that the solution changes in the limits of $\beta \to 0$ (a horizontal channel) and $\beta \to \pi/2$ (a vertical channel). Repeating the analysis for a horizontal channel shows that in this case $A = O(\alpha^{-7})$ (Floryan & Floryan 2015) while for a vertical channel $A = O(\alpha^{-5})$ (Floryan *et al.* 2023*d*).

To deduce the Nusselt number, we start by looking at the solution (6.12). It would be expected that the leading-order Nusselt number would be

$$\alpha^{-2}\left.\frac{\mathrm{d}\hat{\Theta}_{3M}}{\mathrm{d}Y}\right|_{Y=0}, \tag{6.21}$$

but it can easily be verified that this quantity actually vanishes. The next-order problem is given by

$$\frac{1}{Pr}(\hat{\Theta}_{4XX} + \hat{\Theta}_{4YY}) = 2Y\,Re\hat{\Theta}_{2X}, \tag{6.22}$$

and we can determine the mean part of the solution. If this mean component is denoted as $\hat{\boldsymbol{\Theta}}_{4\boldsymbol{M}}(\boldsymbol{Y})$ then

$$\hat{\Theta}_{4M} = -\tfrac{1}{512}Y(Ra_{p,L}^2 + Ra_{p,R}^2)\cos\beta \tag{6.23}$$

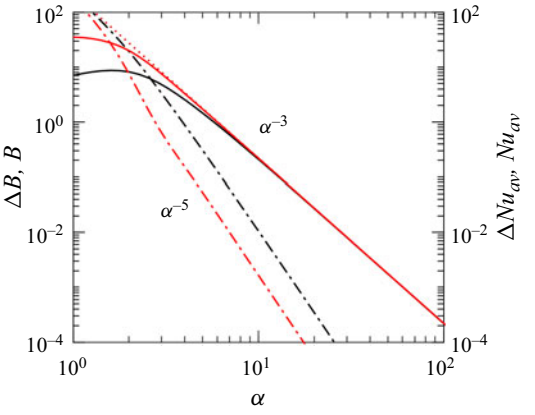


Figure 14. The form of the pressure-gradient correction $B$ (black lines) and the average Nusselt number $Nu_{av}$ (red lines). Solid lines denote numerically determined values, while the dotted lines indicate the analytical values as given by (6.20) and (6.24). Calculations performed with parameter values $Re = 1$, $Ra_{p,R} = 400$ and $Ra_{p,L} = 0$. The dashed-dotted lines denote the differences $\Delta B$ and $\Delta Nu$ between the numerical and analytical predictions.

by matching directly with the core-layer solution. Hence, the Nusselt number becomes

$$\alpha^{-3}\frac{\mathrm{d}\hat{\Theta}_{4M}}{\mathrm{d}Y}\bigg|_{Y=0} = -\alpha^{-3}\left\{\frac{1}{512}(Ra_{p,L}^2 + Ra_{p,R}^2)\cos\beta\right\}. \tag{6.24}$$

The above discussion shows that to maintain a constant mass flux through the channel exposed to the heating, we need to impose a pressure-gradient correction $B = \alpha^{-3}A$, where $A$ is given by (6.20). The resulting heat flow between the walls is given by (6.24). In figure 14, we compare our asymptotic predictions with some numerical simulations; excellent agreement is observed between the two cases for $\alpha > 10$.

## 7. Discussion

An investigation has been conducted into the changes in pressure losses within an inclined channel induced by applying patterned heating to one or both boundaries. A combination of asymptotic analysis and spectrally accurate numerical tools has enabled us to probe the details of the flow and thermal structures that arise. As may have been anticipated, patterned heating leads to intricate flow and temperature field topologies, and a central pillar of these structures involves the formation of separation bubbles. These bubbles mitigate the direct contact between the stream and the side walls, thereby reducing friction experienced by the stream. Fluid rotation inside the bubbles, driven by longitudinal temperature gradients, also reduces resistance. On the other hand, the flow blockage associated with the bubbles tends to increase the flow resistance. The slightly subtle interplay of these three effects determines whether overall there is a net increase or decrease in the resistance. We have already noted that at a sufficiently large flow Reynolds number, the separation bubbles are completely washed away; the upshot is that a relatively simple temperature field remains while the drag-reducing effect has been removed.

A complex temperature field leads to the formation of a rather intricate buoyancy field. We have seen that the longitudinal component of the mean buoyancy force plays the dominant role in the flow response. Since this vanishes when the channel is horizontal, it is unsurprising that the effect of patterned heating on inclined channels is rather more

than a simple modification of the previously known horizontal results. The form of the pressure loss is a function of the channel orientation and the heating wavenumber. When only one wall is heated, the reduction in the pressure gradient can be so significant that an opposite-signed gradient must be applied to prevent flow acceleration. With all other parameters held fixed, the pressure loss seemed to be small in channels oriented not too far from horizontal and increased in channels oriented closer to vertical. For fixed heating intensities, the largest pressure correction occurs at some $O(1)$ heating wavenumber; moreover, it reduces proportional to $\alpha^2$ as $\alpha \to 0$ and to $\alpha^{-3}$ when $\alpha \to \infty$. For relatively weak heating intensity, the size of the pressure-gradient correction is proportional to the square of the Rayleigh number, but much stronger heating leads to a saturation effect.

We reiterate that all our computations were conducted with $Pr = 0.71$. We claimed that the main findings are independent of the choice of $Pr$, and this is at least partially borne out by the asymptotic results (5.13) and (6.20) relating to the long- and short-wavelength modes. It is clear that changes in $Pr$ would change quantitative details but have no major effect on the overall flow structure. It would only be in the cases of exceptionally large or small Prandtl numbers that more significant changes are likely to be seen.

We have also investigated the pressure reductions achieved by heating both walls. In particular, we have focused on the role played by the phase difference when the two walls are heated with the same intensities. Very significant pressure reductions can be achieved if the heating patterns are positioned optimally. Of course, our findings could be extended to account for the situation when the two walls experience different degrees of heating. A series of simulations suggest that, in this case, the various structures are reminiscent of the results described above. If one surface is heated appreciably more strongly than the other, the results seem to be qualitatively similar to the one-wall heating case described in § 3.

It is important to emphasize that we do not necessarily claim a net reduction in energy consumption. Our assertions are rather more modest; although we have shown conclusively that heating reduces pressure losses, it is not straightforward to make definitive statements regarding the implications for the overall energy budget. The cost of generating temperature patterns required to reduce flow losses is very problem-specific but is independent of the fluid mechanics. There are literally hundreds of possible ways to generate the required wall temperature distribution so it is difficult to determine the energy cost without knowing the details of wall construction. The energy losses are associated with heat transfer across the channel and conduction along the wall. This second process is likely to prove critical as it takes energy to maintain longitudinal temperature gradients along the wall. To complicate matters, waste heat is often available, so a discussion of the energy cost of flow actuation becomes somewhat moot as waste energy costs almost nothing. Clearly, there is much scope in assessing the practical implications of our suggested mechanism.

There is a limit to the available pressure gradient required to produce the desired flow rate. This limit could be dictated by technological limitations in producing such pressure differences (e.g. pump limitations) or by structural limitations, as an excessive pressure difference between channel interior and exterior may lead to structural deformations. In these cases, one may want to look at a distributed pumping mechanism, which can be created using heating patterns. In such situations, the energy cost is irrelevant, and obtaining a proper flow rate is key. A combination of heating with the existing propulsion methods can provide performance that is not otherwise available. In this context, the results summarized in Floryan (2023) suggest mechanisms that lead to an expected net energy reduction.

We intend to continue exploring this problem, and should important new structures become evident, we shall report on them in due course. One also needs to verify the stability properties of the flow, as the appearance of any secondary flow would modify the predictions reported in this paper. Computations for the formation of secondary flows in horizontal channels suggest that it does not occur until the Rayleigh number exceeds 2500, a value somewhat larger than those examined in the current work. Furthermore, simple physical arguments suggest that the critical Rayleigh number required to form secondary flows should increase with the inclination angle.

**Acknowledgements.** We are extremely grateful to the anonymous referees whose numerous comments have led to a significantly improved paper. The authors would like to thank Mr S.A. Aman for carrying out part of the required computations.

**Funding.** This work has been carried out with support from NSERC of Canada.

**Declaration of interests.** The authors report no conflict of interest.

**Author ORCIDs.**
J.M. Floryan https://orcid.org/0000-0003-3296-4122;
W. Wang https://orcid.org/0000-0001-8547-2047;
Andrew P. Bassom https://orcid.org/0000-0003-3275-7801.

## References

Abtahi, A. & Floryan, J.M. 2017*a* Natural convection in corrugated slots. *J. Fluid Mech.* **815**, 537–569.
Abtahi, A. & Floryan, J.M. 2017*b* Natural convection and thermal drift. *J. Fluid Mech.* **826**, 553–582.
Abtahi, A. & Floryan, J.M. 2018 On the formation of thermal drift. *Phys. Fluids* **30**, 043602.
Aljallis, E., Sarshar, M.A., Datla, R., Sikka, V., Jones, A. & Choi, C.H. 2013 Experimental study of skin friction drag reduction on superhydrophobic flat plates in high Reynolds number boundary layer flow. *Phys. Fluids* **25**, 025103.
Andreozzi, A., Buonomo, B. & Manca, O. 2005 Numerical study of natural convection in vertical channels with adiabatic extensions downstream. *Numer. Heat Transfer* A*: Applics* **47**, 741–762.
Batchelor, G.K. 1954 Heat transfer by free convection across a closed cavity between vertical boundaries at different temperatures. *Q. Appl. Maths* **XII**, 209–233.
Bewley, R. 2009 A fundamental limit on the balance of power in a transpiration-controlled channel flow. *J. Fluid Mech.* **632**, 443–446.
Bocquet, L. & Lauga, E. 2011 A smooth future? *Nat. Mater.* **10**, 334–337.
Floryan, D. 2023 A fundamental limit on energy savings in controlled channel flow, and how to beat it. *J. Fluid Mech.* **954**, R3.
Floryan, D. & Floryan, J.M. 2015 Drag reduction in heated channels. *J. Fluid Mech.* **765**, 353–395.
Floryan, J.M., Aman, S.A. & Panday, S. 2024 Use of heated corrugations for propulsion. *J. Fluid Mech.* **980**, A41.
Floryan, J.M., Benayoun, A., Panday, S. & Bassom, A.P. 2022*a* Patterned convection in inclined slots. *J. Fluid Mech.* **950**, A11.
Floryan, J.M. & Haq, H. 2022 Use of vibrations for reduction of resistance in relative movement of parallel plates. *J. Fluid Mech.* **949**, A28.
Floryan, J.M., Haq, N. & Bassom, A.P. 2023*a* On fast peristaltic waves. *Eur. J. Mech.* (B/*Fluids*) **100**, 239–246.
Floryan, J.M., Haq, N. & Bassom, A.P. 2023*b* The propulsive effect generated by fast travelling-wave vibrations. *Acta Mechanica* **234**, 5039–5052.
Floryan, J.M., Haq, H. & Panday, S. 2022*b* Horizontal chimney effect. *Trans. ASME J. Heat Transfer* **144**, 072601.
Floryan, J.M. & Inasawa, A. 2021 Pattern interaction effect. *Sci. Rep.* **11**, 14573.
Floryan, J.M., Panday, S. & Aman, S.A. 2023*c* Propulsion due to thermal streaming. *J. Fluid Mech.* **967**, A13.
Floryan, J.M., Shadman, S. & Hossain, M.Z. 2018 Heating-induced drag reduction in relative movement of parallel plates. *Phys. Rev. Fluids* **3**, 094101.

FLORYAN, J.M., WANG, W. & BASSOM, A.P. 2023*d* The reduction of pressure losses in thermally-modulated vertical channels. *J. Fluid Mech.* **954**, A38.
FLORYAN, J.M., WANG, W., PANDAY, S. & BASSOM, A.P. 2022*c* Natural convection and pattern interaction in a two-dimensional vertical slot. *J. Fluid Mech.* **946**, A20.
FLORYAN, J.M. & ZANDI, S. 2019 Reduction of pressure losses and increase of mixing in laminar flows through channels with long-wavelength vibrations. *J. Fluid Mech.* **864**, 670–707.
FUKAGATA, K., SUGIYAMA, K. & KASAGI, N. 2009 On the lower bound of net driving power in controlled duct flows. *Physica* D **238**, 1082–1086.
FUKUNISHI, Y. & EBINA, I. 2001 Active control of boundary-layer transition using a thin actuator. *JSME Intl J.* **44**, 24–29.
HALL, P. 2012 Vortex-wave interactions: long wavelength streaks and spatial localization in natural convection. *J. Fluid Mech.* **703**, 99–110.
HAQ, N.N. & FLORYAN, J.M. 2022 Propulsive effect of wall vibrations. *ASME J. Fluid Engng* **144**, 121204.
HAQ, N.N. & FLORYAN, J.M. 2023 Effects of wall vibrations on channel flows. *J. Fluid Mech.* **968**, A8.
HOEPFFNER, J. & FUKAGATA, K. 2009 Pumping or drag reduction? *J. Fluid Mech.* **635**, 171–187.
HOSSAIN, M.Z. & FLORYAN, J.M. 2013*a* Heat transfer due to natural convection in a periodically heated slot. *Trans. ASME J. Heat Transfer* **135**, 022503.
HOSSAIN, M.Z. & FLORYAN, J.M. 2013*b* Instabilities of natural convection in a periodically heated layer. *J. Fluid Mech.* **733**, 33–67.
HOSSAIN, M.Z. & FLORYAN, J.M. 2014 Natural convection in a fluid layer periodically heated from above. *Phys. Rev.* E **90**, 023015.
HOSSAIN, M.Z. & FLORYAN, J.M. 2015*a* Natural convection in a horizontal fluid layer periodically heated from above and below. *Phys. Rev.* E **92**, 023015.
HOSSAIN, M.Z. & FLORYAN, J.M. 2015*b* Mixed convection in a periodically heated channel. *J. Fluid Mech.* **768**, 51–90.
HOSSAIN, M.Z. & FLORYAN, J.M. 2016 Drag reduction in a thermally modulated channel. *J. Fluid Mech.* **791**, 122–153.
HOSSAIN, M.Z. & FLORYAN, J.M. 2020 On the role of surface grooves in the reduction of pressure losses in heated channels. *Phys. Fluids* **32**, 083610.
HOSSAIN, M.Z. & FLORYAN, J.M. 2022 Wavenumber lock-in and spatial parametric resonance in convection. *J. Fluid Mech.* **944**, A47.
HOSSAIN, M.Z. & FLORYAN, J.M. 2023 Pumping using thermal waves. *J. Fluid Mech.* **966**, A43.
HOSSAIN, M.Z., FLORYAN, D. & FLORYAN, J.M. 2012 Drag reduction due to spatial thermal modulations. *J. Fluid Mech.* **713**, 398–419.
HUGHES, G.O. & GRIFFITHS, R.W. 2008 Horizontal convection. *Annu. Rev. Fluid Mech.* **40**, 185–208.
INASAWA, A., HARA, K. & FLORYAN, J.M. 2021 Experiments on thermal drift. *Phys. Fluids* **33**, 087116.
INASAWA, A., NINOMIYA, C. & ASAI, M. 2013 Suppression of tonal trailing-edge noise from an airfoil using a plasma actuator. *AIAA J.* **51**, 1695–1702.
INASAWA, A., TANEDA, K. & FLORYAN, J.M. 2019 Experiments on flows in channels with spatially distributed heating. *J. Fluid Mech.* **872**, 177–197.
JIANG, H., ZHU, X., MATHAI, V., YANG, X., VERZICCO, R., LOHSE, D. & SUN, C. 2019 Convective heat transfer along ratchet surfaces in vertical natural convection. *J. Fluid Mech.* **873**, 1055–1071.
JIAO, L. & FLORYAN, J.M. 2021*a* On the use of transpiration for reduction of resistance to relative movement of parallel plates. *Phys. Rev. Fluids* **6**, 014101.
JIAO, L. & FLORYAN, J.M. 2021*b* On the use of transpiration patterns for reduction of pressure losses. *J. Fluid Mech.* **915**, A78.
JOSEPH, P., COTTIN-BIZONNE, C., BENOIT, J.M., YBERT, C., JOURNET, C., TABELING, P. & BOCQUET, L. 2006 Slippage of water past superhydrophobic carbon nanotube forests in microchannels. *Phys. Rev. Lett.* **97**, 156104.
KATO, T., FUKUNISHI, Y. & KOBAYASHI, R. 1997 Artificial control of the three-dimensionalization process of T-S waves in boundary-layer transition. *JSME Intl J.* **40**, 536–541.
LEE, Y. & KORPELA, S.A. 1983 Multicellular natural convection in a vertical slot. *J. Fluid Mech.* **126**, 91–121.
LINDEN, P.F. 1999 The fluid mechanics and natural ventilation. *Annu. Rev. Fluid Mech.* **31**, 201–238.
MAMORI, H., IWAMOTO, K. & MURATA, A. 2014 Effect of the parameters of traveling waves created by blowing and suction on the relaminarization phenomena in fully developed turbulent channel flow. *Phys. Fluids* **26**, 015101.
MAXWORTHY, T. 1997 Convection into domains with open boundaries. *Annu. Rev. Fluid Mech.* **29**, 327–371.
MAYELI, P. & SHEARD, G.J. 2021 Buoyancy-driven flows beyond the Boussinesq approximation: a brief review. *Intl Commun. Heat Mass Transfer* **125**, 105316.

MIN, T., KANG, S.M., SPEYER, J.L. & KIM, J. 2006 Sustained sub-laminar drag in a fully developed channel flow. *J. Fluid Mech.* **558**, 309–318.
MOHAMMADI, A. & FLORYAN, J.M. 2012 Mechanism of drag generation by surface corrugation. *Phys. Fluids* **24**, 013602.
MOHAMMADI, A. & FLORYAN, J.M. 2013*a* Pressure losses in grooved channel. *J. Fluid Mech.* **725**, 23–54.
MOHAMMADI, A. & FLORYAN, J.M. 2013*b* Groove optimization for drag reduction. *Phys. Fluids* **25**, 113601.
MOHAMMADI, A. & FLORYAN, J.M. 2014 Effects of longitudinal grooves on the Couette–Poiseuille flow. *J. Theor. Comput. Fluid Dyn.* **28**, 549–572.
MOHAMMADI, A. & FLORYAN, J.M. 2015 Numerical analysis of laminar-drag-reducing grooves. *Trans. ASME J. Fluids Engng* **137**, 041201.
MOHAMMADI, A., MORADI, H.V. & FLORYAN, J.M. 2015 New instability mode in a grooved channel. *J. Fluid Mech.* **778**, 691–720.
MORADI, H.V. & FLORYAN, J.M. 2013 Flows in annuli with longitudinal grooves. *J. Fluid Mech.* **716**, 280–315.
MORADI, H.V. & FLORYAN, J.M. 2014 Stability of flow in a channel with longitudinal grooves. *J. Fluid Mech.* **757**, 613–648.
MORTENSEN, D.K., WALKER, I.S. & SHERMAN, M. 2011 Energy and air quality implications of passive stack ventilation in residential buildings. *Ernest Orlando Lawrence Berkeley National Laboratory Report* LBNL-4589E.
NAGLER, J. 2021 Numerical simulation of a mixed vertical ventilation system. *Z. Angew. Math. Mech.* **101**, e201900353.
NAYLOR, D., FLORYAN, J.M. & TARASUK, J.D. 1991 A numerical study of developing free convection between isothermal vertical plates. *Trans. ASME J. Heat Transfer* **113**, 620–626.
NG, C.S., OOI, A., LOHSE, D. & CHUNG, D. 2015 Vertical natural convection: application of the unifying theory of thermal convection. *J. Fluid Mech.* **764**, 349–361.
NOVAK, M. & FLORYAN, J.M. 1995 Free convection in systems of vertical channels. *Intl J. Heat Fluid Flow* **16**, 244–253.
OU, J., PEROT, J.B. & ROTHSTEIN, J.P. 2004 Laminar drag reduction in microchannels using ultrahydrophobic surfaces. *Phys. Fluids* **16**, 4635.
PARK, H., PARK, H. & KIM, J. 2013 A numerical study of the effects of superhydrophobic surface on skin-friction drag in turbulent channel flow. *Phys. Fluids* **25**, 110815.
PARK, H., SUN, G. & KIM, J. 2014 Superhydrophobic turbulent drag reduction as a function of surface grating parameters. *J. Fluid Mech.* **747**, 722–734.
POETES, R., HOLTZMANN, K., FRANZE, K. & STEINER, U. 2010 Metastable underwater superhydrophobicity. *Phys. Rev. Lett.* **105**, 166104.
PUTNAM, J.O. 1882 *The Open Fire for All Ages*. James R. Osgood and Company.
QUÉRÉ, D. 2008 Wetting and roughness. *Annu. Rev. Mater. Res.* **38**, 71–99.
REYSSAT, M., YEOMANS, J.M. & QUÉRÉ, D. 2008 Impalement of fakir drops. *Europhys. Lett.* **81**, 26006.
ROSENBERG, J., VAN BUREN, T., FU, M.K. & SMITS, A.J. 2016 Turbulent drag reduction over air- and liquid impregnated surfaces. *Phys. Fluids* **28**, 015103.
ROTHSTEIN, J.P. 2010 Slip on superhydrophobic surfaces. *Annu. Rev. Fluid Mech.* **42**, 89–109.
SAMAHA, M.A., TAFRESHI, H.V. & GAD-EL-HAK, M. 2011 Modeling drag reduction and meniscus stability of superhydrophobic surfaces comprised of random roughness. *Phys. Fluids* **23**, 012001.
SAMAHA, M.A., TAFRESHI, H.V. & GAD-EL HAK, M. 2012 Influence of flow on longevity of superhydrophobic coatings. *Langmuir* **28**, 9759–9766.
SHAHIN, G.A. & FLORYAN, J.M. 1999 Heat transfer enhancement generated by the chimney effect in systems of vertical channels. *Trans. ASME J. Heat Transfer* **121**, 230–232.
SHISHKINA, O. & WAGNER, C. 2011 Modelling the influence of wall roughness on heat transfer in thermal convection. *J. Fluid Mech.* **686**, 568–582.
SIGGERS, J.H., KERSWELL, R.R. & BALMFORTH, N.J. 2004 Bounds on horizontal convection. *J. Fluid Mech.* **517**, 55–70.
SOLOMON, B.R., KHALIL, K.S. & VARANASI, K.K. 2014 Drag reduction using lubricant-impregnated surfaces in viscous laminar flow. *Langmuir* **30**, 10970–10976.
SOLOMON, B.R., KHALIL, K.S. & VARANASI, K.K. 2016 Correction to drag reduction using lubricant-impregnated surfaces in viscous flows. *Langmuir* **32**, 8287–8287.
SONG, Z., HUANG, X., KUENZER, C., ZHU, H., JIANG, J., PAN, X. & ZHONG, F. 2020 Chimney effect induced by smoldering fire in a U-shaped porous channel: a governing mechanism of the persistent underground coal fires. *Process Saf. Environ. Prot.* **136**, 136–147.
SRINIVASAN, S., CHOI, W., PARK, K.C.L., CHATRE, S.S., COHEN, R.E. & MCKINLEY, G.H. 2013 Drag reduction for viscous laminar flow on spray-coated non-wetting surfaces. *Soft Matt.* **9**, 5691–5702.

STRAATMAN, A.G., NAYLOR, D., TARASUK, J.D. & FLORYAN, J.M. 1994 Free convection between inclined isothermal plates. *Trans. ASME J. Heat Transfer* **116**, 243–245.

STRAATMAN, A.G., TARASUK, J.D. & FLORYAN, J.M. 1993 Heat transfer enhancement from a vertical, isothermal channel generated by the chimney effect. *Trans. ASME J. Heat Transfer* **115**, 395–402.

TOPPALADODDI, S., SUCCI, S. & WETTLAUFER, J.S. 2017 Roughness as a route to the ultimate regime of thermal convection. *Phys. Rev. Lett.* **118**, 074503.

TOURNIER, C., GETHON, P. & RABINOWICZ, M. 2000 The onset of natural convection in vertical fault planes: consequences for the thermal regime in crystalline basements and for heat recovery experiments. *Geophys. J. Intl* **140**, 500–508.

TRITTON, D.J. 1977 *Physical Fluid Dynamics*. Springer Dordrecht.

TRUESDELL, R., MAMMOLI, P., VOROBIEFF, P., VAN SWOL, P. & BRINKER, C.J. 2006 Drag reduction on a patterned superhydrophobic surface. *Phys. Rev. Lett.* **97**, 044504.

VAN BUREN, T. & SMITS, A.J. 2017 Substantial drag reduction in turbulent flow using liquid-infused surface. *J. Fluid Mech.* **827**, 448–456.

VEST, C.M. & ARPACI, V.S. 1969 Stability of natural convection in a vertical slot. *J. Fluid Mech.* **36**, 1–15.

WALSH, M.J. 1983 Riblets as a viscous drag reduction technique. *AIAA J.* **21**, 485–486.

WEIL, A. 2012 *Nuclear Power. Practical Aspects*. IntechOpen Book Series.

WINTERS, K.B. & YOUNG, W.R. 2009 Available potential energy and buoyancy variance in horizontal convection. *J. Fluid Mech.* **629**, 221–230.

WONG, N.H. & HERYANTO, S. 2004 The study of active stack effect to enhance natural ventilation using wind tunnel and computational fluid dynamics (CFD) simulations. *Energy Build.* **36**, 668–678.

WONG, T.S., KANG, S.H., TANG, S.K.Y., SMYTHE, E.J., HATTON, B.D., GRINTHAL, A. & AIZENBERG, J. 2011 Bioinspired self-repairing slippery surfaces with pressure-stable omniphobicity. *Nature* **477**, 443–447.

ZELDOVICH, Y.B. 1937 Limiting laws of freely rising convection currents. *Zhurnal Eksperimentalnoyi i Teoreticheskoyi Fizika* **7**, 1463–1465.

ZHOU, M., LI, J., WU, C., ZHOU, X. & CAI, L. 2011 Fluid drag reduction on superhydrophobic surfaces coated with carbon nanotube forest (CNTs). *Soft Matt.* **7**, 4391–4396.